Model-Based Optimization of Hydrogen Generation by Methane Steam Reforming in Autothermal Packed-Bed Membrane Reformer

David S. A. Simakov and Moshe Sheintuch
Dept. of Chemical Engineering, Technion-Israel Institute of Technology, Haifa 32000, Israel

DOI 10.1002/aic.12265
Published online April 28, 2010 in Wiley Online Library (wileyonlinelibrary.com).

An autothermal membrane reformer comprising two separated compartments, a methane oxidation catalytic bed and a methane steam reforming bed, which hosts hydrogen separation membranes, is optimized for hydrogen production by steam reforming of methane to power a polymer electrolyte membrane fuel cell (PEMFC) stack. Capitalizing on recent experimental demonstrations of hydrogen production in such a reactor, we develop here an appropriate model, validate it with experimental data and then use it for the hydrogen generation optimization in terms of the reformer efficiency and power output. The optimized reformer, with adequate hydrogen separation area, optimized exothermic-to-endothermic feed ratio and reduced heat losses, is shown to be capable to fuel kW-range PEMFC stacks, with a methane-to-hydrogen conversion efficiency of up to 0.8. This is expected to provide an overall methane-to-electric power efficiency of a combined reformer-fuel cell unit of ~0.5. Recycling of steam reforming effluent to the oxidation bed for combustion of unreacted and unseparated compounds is expected to provide an additional efficiency gain. © 2010 American Institute of Chemical Engineers *AIChE J,* 57: 525–541, 2011

Keywords: hydrogen, methane steam reforming, membrane reactor, autothermal reformer, optimization, fuel cells

Introduction

Hydrogen is a very promising environmentally friendly fuel, its combustion in fuel cells directly produces electricity in a pollution-free way with efficiency (claimed to be 60% for PEM fuel cells) that is much higher than that of heat engines (30% and lower). The high energy transformation efficiency of fuel cells may decrease significantly carbon dioxide emission, even when fossil fuels are still used as a source of hydrogen. Conventionally, hydrogen production is carried out by the industrial-scale steam reforming of natural gas, which is a multistage process that includes several reactions (and catalysts), with heat-exchange between them (steam reforming is highly endothermic), followed by hydrogen separation.

In addition, unless produced on-site, hydrogen has to be compressed or liquefied, stored, transported, and distributed to the end user. This, and the complexity and high energy demand of the conventional hydrogen generation processes, reduces significantly the overall efficiency of the hydrogen-based energy pathway, making the price of hydrogen uneconomical. On-board high-purity hydrogen generation from natural gas by a portable autothermal membrane reformer, combining exothermic and endothermic reactions, is a very promising approach that can save costs of hydrogen storage and distribution. Such a process should combine two reactors

Correspondence concerning this article should be addressed to M. Sheintuch at cermsll@technion.ac.il.

(reformer and combustor), heat exchange between them and hydrogen separation into one compact and thermally independent unit. For the autothermal packed bed membrane reformer to be economical and practical, its energetic efficiency should be better then the ratio of combustion engine efficiency (<30%) to fuel cell efficiency (~60%), and its power density (power to volume ratio) should be at least similar to that of PEM fuel cells (~1 kW/L).

As there are large resources of natural gas in the world, steam reforming of methane is of notable interest. The methane steam reforming (MSR) process is commonly described by three reactions: methane conversion to H_2 and CO (Eq. 1), the water gas shift (WGS, Eq. 2), and the direct (overall) MSR reaction (Eq. 3).

$$CH_4 + H_2O = CO + 3H_2 \quad \Delta H_1 = 206\,\mathrm{kJ/mol} \qquad (1)$$

$$CO + H_2O = CO_2 + H_2 \quad \Delta H_2 = -41\,\mathrm{kJ/mol} \qquad (2)$$

$$CH_4 + 2H_2O = CO_2 + 4H_2 \quad \Delta H_3 = 165\,\mathrm{kJ/mol} \qquad (3)$$

We briefly review pertinent information on elements of such a process. Numerical[1–6] and experimental[7–15] investigation of hydrogen generation by MSR, using membrane reformers, has been reported in many works. A packed bed membrane reactor (PBMR)[1–3,5–10] and a fluidized bed membrane reactor (FBMR)[4,11–15] are commonly used. As the membrane reformer performance is limited by separation rate, the optimization of membrane transport properties (permeability to hydrogen) is one of the important issues in the developing of membrane reactor technologies.

Membranes composed of a Pd-Ag thin layer on a ceramic or stainless steel porous supports[8–10] are very promising, as they exhibit higher permeabilities than that of Pd-Ag foil membranes. As the Pd cost is prohibitive, other substitutes with good selectivity for hydrogen separation, like carbon,[16,17] silica,[18,19] and zeolitic[20,21] hydrogen-separation membranes have been extensively investigated, but they still cannot produce the desired selectivity and durability.

The high endothermicity of the MSR process remains one of the major drawbacks in its implementation for portable hydrogen generation. The membrane reformer has to be coupled to a heat source, which is commonly done in experimental works either completely[7–12] or partially[13–15] by electrical heaters. Renewable energy sources, such as solar energy,[22] can be also used for this purpose, but mostly for stationary applications as it requires quite bulky additional equipment. Coupling MSR to an exothermic reaction, such as methane oxidation (Eq. 4)[4–6,13–15] or hydrogen oxidation[13] is a prerequisite if it is aimed to design a portable, thermally independent system.

$$CH_4 + 2O_2 = CO_2 + 2H_2O \quad \Delta H_{Ox} = -803\,\mathrm{kJ/mol} \qquad (4)$$

The thermal reactive coupling can be performed directly, by performing endothermic and exothermic reactions over the same catalyst bed (e.g., autothermal steam reforming, ATR[14,15]), or indirectly, using heat exchange reactors.[5,6] When air is used as an oxygen source for ATR in a membrane reactor, nitrogen dilutes the reactive stream, suppressing the hydrogen separation due to diminished hydrogen partial pressure gradient. As using pure oxygen is not a practical approach, this appears to be an inherent disadvantage of the direct coupling approach. In addition, using air for supplying oxygen will increase the reactor dimensions; air also has to be compressed to the pressures required to drive hydrogen separation. Furthermore, finding a good catalyst for the three reactions may be quite difficult: MSR is typically conducted with Ni, whereas MOx is usually conducted on noble metals.

The indirect coupling version, where the exothermic and endothermic reactions are separated in space, while being less efficient for heat transfer, is free from the direct coupling shortcomings discussed above. The indirect coupling also enables operational flexibility, because the operating parameters of exothermic and endothermic compartments can be independently adjusted. Numerical simulations of this approach have been reported by Patel and Sunol,[5] simulating the oxidation compartment as a thin layer next to the wall of a packed bed MSR compartment. We have reported the simulations of the indirectly coupled autothermal membrane reformer,[6] where hydrogen separation and the endothermic and exothermic reactions are carried out in concentric tubes, in a way similar to the experimental tests and the model presented here.

In recent publications[23,24] we have demonstrated the feasibility of hydrogen generation in a completely autothermal packed bed membrane methane steam reformer. The reformer was composed of three separated compartments: a MOx catalytic bed, a MSR catalytic bed, and a hydrogen separation membrane. A detailed parametric study was performed[23] and the hydrogen generation optimization was experimentally demonstrated.[24] Yet, the reactor efficiencies (η, defined below) were lower than 20%.

This study is aimed at model-based optimization of the reformer power output and its efficiency. A previously suggested adiabatic model[6] is modified for that purpose in the next section by accounting for heat losses and by using more realistic heat transfer parameters; the model is validated by comparison with experimental results and then in section *Model extension* it is used for studying two optimization strategies. In section *Design limits* we plot various design limits of the model. In section *Thermodynamic optimization algorithm* an approximate analytical solution is suggested to determine the operation window and to find the best operation conditions and a design algorithm is suggested and applied.

Autothermal Packed Bed Membrane Reformer Model

Reactor model. The reactor (see Figure 1 for schematic representation) was simulated as a pseudo-homogeneous 1D system. The simulated reactor comprises of two concentric cylindrical compartments: for oxidation (Ox) on the outside and for steam reforming (SR) in the inner compartment, with the latter equipped with one or several hydrogen separation membranes (all in the $0 < z < L$ domain). The experimental system is detailed elsewhere,[23,24] but it includes the same compartments: the inner hydrogen separation membrane, the intermediate bed packed with Ni/Al_2O_3 (SG-9301, 16.5 wt % NiO, *Engelhard*) bounded with (316SS) wall for MSR and an outer tube (316 SS) packed with Pt/Al_2O_3

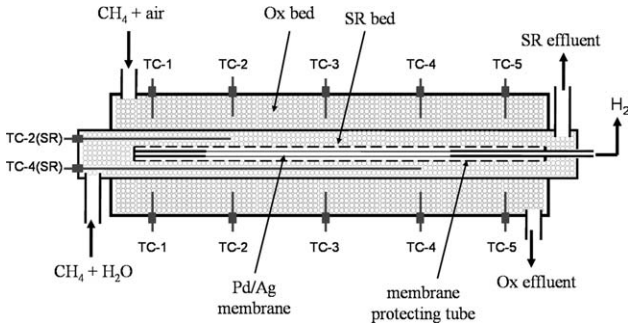

Figure 1. Schematic of the membrane reformer showing the three compartments: Ox, oxidation; SR, steam reforming; TC, thermocouple.

(0.5 wt % Pt, Johnson Matthey) for MOx. A tubular heater was wrapped around the Ox compartment to facilitate start-up and the whole reactor was covered with a thermal insulation layer. Two commercially available membranes were experimentally tested: (i) Pd-Ag foil, Johnson Matthey (JM, UK) and (ii) Pd-Ag supported film (Inconel support), REB Research & Consulting (REB, US). The experimental unit dimensions and membrane characteristics are listed in Tables 1 and 2. In the model, as in the experiments, a 10 bar pressure and an atmospheric pressure are maintained in the SR compartment and the Ox compartments, respectively, while the membrane inner pressure is kept at 0.1 bar, in agreement with some of the experiments (an atmospheric pressure was maintained in others).

A standard transient pseudo-homogeneous model with axial convection and thermal and mass dispersion terms is used, with hydrogen permeation following Sievert's law (Eq. 6a). The interphase transfer effects were included through the axial thermal and mass dispersion terms. Although heterogeneous model would be expected to provide a more accurate solution, the model validation versus experimental data (with no adjustable parameters) provided an acceptable agreement (section *Numerical solution validation*). The model takes the following form:

$$(\rho C_p)_e^k \frac{\partial T^k}{\partial t} = k_{ax}^k \frac{\partial^2 T^k}{\partial z^2} - \varepsilon^k (\rho v C_p)_g^k \frac{\partial T^k}{\partial z} + \rho_s^k (1-\varepsilon^k) \sum_j (-\Delta H_j) R_j - (a_v^k U_w \Delta T^k)_{HE} - (a_v^k U_w \Delta T^k)_{HL} \quad (5)$$

$$(\varepsilon \rho_g)^k \frac{\partial y_i^k}{\partial t} = (\rho_g D_{ax})^k \frac{\partial^2 y_i^k}{\partial z^2} - (\varepsilon \rho_g v_g)^k \frac{\partial y_i^k}{\partial z} + \rho_s^k (1-\varepsilon^k) \sum_j \alpha_{ij} R_j - a_{v,M}^k J_i^k \quad (6)$$

$$J_i^k = A_i \exp\left(\frac{-E_{H_2}}{R_g T^k}\right) \Delta\left(\sqrt{p_i}\right)^k \quad (6a)$$

The index $k = M, SR, Ox$ denotes the compartment, the index $i = CH_4, O_2, H_2O, CO, CO_2, H_2$ denotes the species, whereas the indexes $j = 1-3$ correspond to the three MSR reactions (Eqs. 1–3) and $j = 4$ to the MOx reaction (Eq. 4). Thus, there are no reactions for $k \equiv M$, while for $k \equiv SR$, reactions $j = 1-3$ apply, etc. The intercompartmental heat exchange (denoted by *HE*) applies for $k \equiv SR, Ox$ with appropriate sign, whereas the heat loss term (denoted by *HL*) applies only to $k \equiv Ox$. Also, $J_i^k = 0$ except for $i = H_2$ and $k \equiv M, SR$. Ideal gas, negligible radial gradients and negligible axial pressure drop are assumed. Note that variations in total molar density have been neglected. Even though Eqs. 1 and 3 predict an increase in the number of moles, in a membrane reactor a significant part of H_2 is separated by the membrane and the total molar density variations are neglected here. Also, an infinite heat transfer coefficient between the membrane interior and the SR compartment is assumed ($T^M = T^{SR}$) and the axial dispersion term in the membrane interior is neglected, i.e., $(p_g D_{ax})^M = 0$. Other definitions include

$$(\rho C_p)_e = (\varepsilon \rho_g C_{pg} + (1-\varepsilon)\rho_s C_{ps}), \quad v_g^k = \frac{Q_{tf}^k}{\varepsilon A_{cs}^k},$$

$$A_i = 0 \text{ for } i \neq H_2$$

$$a_{v,HE}^k = \frac{S^{SR}}{V^k}, \quad a_{v,HL}^k = \frac{S^{Ox}}{V^{Ox}}, \quad a_{v,M}^k = \frac{S^M}{V^k}$$

$$\Delta T_{HE}^{SR} = T^{SR} - T^{Ox}, \quad \Delta T_{HE}^{Ox} = -\Delta T_{HE}^{SR},$$

$$\Delta T_{HL}^{SR} = 0, \quad \Delta T_{HL}^{Ox} = T^{Ox} - T_a$$

$$\Delta\left(\sqrt{p_i}\right)^{SR} = \sqrt{p_i^{SR}} - \sqrt{p_i^M}, \quad \Delta\left(\sqrt{p_i}\right)^M = -\Delta\left(\sqrt{p_i}\right)^{SR},$$

$$p_i^k = y_i^k P_t^k$$

The boundary (Danckwert's) and initial conditions are:

$$z = 0: \quad \varepsilon^k (\rho v C_p)_g^k (T_f^k - T^k) = -k_{ax}^k \frac{\partial T^k}{\partial z}$$

$$\varepsilon^k (\rho v)_g^k (y_{if}^k - y_i^k) = -(\rho_g D_{ax})^k \frac{\partial y_i^k}{\partial z} \quad (7a)$$

$$z = L: \quad \frac{\partial T^k}{\partial z} = 0; \quad \frac{\partial y_i^k}{\partial z} = 0 \quad (7b)$$

$$t = 0: \quad T^k(0,z) = T_{int}^k; \quad y_i^k(0,z) = y_{i,int}^k \quad (8)$$

Table 1. Experimental Unit Dimensions

Section	L(active) (mm)	D (mm)	d_w, (mm)	d_p (mm)
SR	220	27	0.9	3–5
Ox	220	60	1.6	4–6

Table 2. Membrane Dimensions and Permeability Characteristics

Membrane	Type	S (cm^2)	L (mm)	D (mm)
A (JM, UK)	Pd-Ag foil	7.5	150	1.6
B (REB, US)	Pd-Ag film (Inconel-supported)	15	150	3.2

Membrane	d (μm)	E_{H_2} (kJ/mol)	A_{H_2} [mol/(m^2 s bar$^{0.5}$)]	Ref.
A (JM, UK)	70	6.6	0.4	JM, UK
B (REB, US)	10	10.7	0.9	REB, US

The model was solved using the MATLAB PDE solver with a second-order accurate spatial discretization, and with the time integration done by the numerical differentiation formulas. As setting the feed hydrogen molar fraction (y_{H_2f}) to zero will lead to unbounded initial rate (see section *Kinetics*), it was set at $y_{H_2f} = \mathbf{10^{-5}}$; it was verified that the solution is insensitive to this value.

Parameters

In the model, thermophysical, kinetic and thermodynamic parameters listed in the literature are used. However, the parameters crucial for reactor thermal management, such as the wall heat loss coefficient ($U_{w,HL}$) and the catalytic bed effective axial conductivity (k_{ax}) are estimated from the experimental data as shown below.

Kinetics

For MSR over a Ni/Al_2O_3 catalyst, the commonly used rate expressions developed by Xu and Froment[25] are used (equilibrium constants, activation energies and adsorption enthalpies can be found in the original article[25]):

$$R_1 = \frac{k_1}{p_{H_2}^{2.5}}\left(p_{CH_4}p_{H_2O} - \frac{p_{H_2}^3 p_{CO}}{K_{eq,1}}\right)\frac{1}{\Gamma^2} \tag{9a}$$

$$R_2 = \frac{k_2}{p_{H_2}}\left(p_{CO}p_{H_2O} - \frac{p_{H_2}p_{CO_2}}{K_{eq,2}}\right)\frac{1}{\Gamma^2} \tag{9b}$$

$$R_3 = \frac{k_3}{p_{H_2}^{3.5}}\left(p_{CH_4}p_{H_2O}^2 - \frac{p_{H_2}^4 p_{CO_2}}{K_{eq,3}}\right)\frac{1}{\Gamma^2} \tag{9c}$$

$$\Gamma = 1 + K_{CO}p_{CO} + K_{H_2}p_{H_2} + K_{CH_4}p_{CH_4} + \frac{K_{H_2O}p_{H_2O}}{p_{H_2}}$$

$$k_j = A_j \exp\left(\frac{-E_j}{R_gT}\right), \quad K_i = B_i \exp\left(\frac{-\Delta H_i}{R_gT}\right)$$

For the MOx reaction, the activation energy reported for methane oxidation on supported Pt catalyst ($E_{Ox} = 86$ kJ/mol) is used.[26] The pre-exponent was extracted from the Ox conversion (f^{Ox}) versus T data provided by the catalyst supplier (Johnson Matthey, UK) by least squares analysis, assuming that the MOx kinetics is 1st-order in methane and the reactor is ideally mixed and isothermal ($A_{Ox} = 5 \times 10^3$ m^3 / (kg s)):

$$R_4 = k_{Ox}\rho_g^{Ox}y_m^{Ox}, \qquad K_{Ox} = A_{Ox}\exp\left(\frac{-E_{Ox}}{R_gT}\right) \tag{10}$$

$$f^{Ox} = \frac{\tau\rho_s A_{Ox}\exp[-E_{Ox}/(R_gT)]}{1 + \tau\rho_s A_{Ox}\exp[-E_{Ox}/(R_gT)]} \tag{10a}$$

Intraparticle and interphase transport limitations

The use of the pseudo-homogeneous model implies absence of intraparticle transport limitations. We checked, therefore, the criteria for ignoring these gradients. To verify that intraparticle diffusion limitation can be ignored, we calculated the Thiele Modulus[27] (for a first order reaction j, $\phi_j^2 = R_h^2\, k_j^V / D_e$) and found for the SR reaction that $\phi_{SR} < 1$ when $T < 650$°C ($D_e = 1.5 \times 10^{-6}$ m) under inlet conditions (the highest SR reaction rate) and for $d_p = 4 \times 10^{-3}$ m, which is about an average size of the catalyst pellets used in our experimental demonstrations.[23,24] Therefore, intraparticle diffusion limitations are not expected in this case, where the reactor temperatures were mostly in the range of 500°C $< T <$ 700°C. The Ox reaction is much faster, but kinetic parameters were obtained by fitting the catalyst manufacturer data (Eq. 10a), which already account for such gradients. To verify that temperature intraparticle gradients may be neglected we calculated the isothermal catalytic pellet criterion ($|\Delta H_j| R_j d_p^2 / (4k_gT) < 0.75TR_g / E_j$ for a reaction j[28,29]) and found that it is satisfied for both MSR and MOx under inlet conditions in the relevant temperature range (500°C $< T <$ 700°C).

To test the presence of the interphase transport limitation we calculated the criteria $|\Delta H_j|\, Rjd_p / (2h_{fs}T) < 0.15TR_g / E_j$ and $R_j d_p / (2y_i\ \rho_g k_c) < 0.15$ for the heat and mass transfer resistances,[29] using the correlated gas-particle transfer coefficients[27] in the range of $h_{fs} \approx 0.5 - 1.2$ *kJ / (m^2 s K)* and $k_c \approx 0.05 - 0.15$ *m / s* for $R_p = 10 - 100$. The calculations showed that for both MSR and MOx ignoring mass transfer resistance is justified for all the relevant operation conditions. On the other hand, the heat transfer film resistance may be significant for $R_p < 20$ (when h_{fs} is relatively low). Yet, the model, which does not account for the interphase heat transport limitation, predicted well the experimental data (section *Numerical solution validation*) and these effects were neglected here.

Transport coefficients

Intercompartmental Wall Heat Transfer. The wall heat transfer coefficient between the SR and Ox compartments is determined from the following (resistances in series) expression:

$$U_{w,HE} = \frac{1}{1/(h_w^{SR}) + d_w^{SR}/(k_w^{SR}) + 1/(h_w^{Ox})} \tag{11}$$

The wall heat transfer coefficients for each reactor compartment (h_w^{Ox}, h_w^{SR}) are estimated from the following correlation[30,31]:

$$Nu_{w,HE} \equiv \frac{h_w d_p}{k_g} = \frac{d_p}{d_t}\left[2Bi_s\frac{k_{rs}}{k_g} + \beta_f(2Bi_s + 8)\right] \tag{12}$$

The correlation accounts for effects of tube-to-particle diameter ratio (d_p / d_t), solid phase thermal conductivity (k_{rs}), effects of fluid velocity, fluid phase radial heat transfer and interphase heat transfer (β_f) and the wall-to-solid heat transfer (Bi_s); expressions for β_f and Bi_s can be found in the original articles.[30,31] Over particle Reynolds number (Re_p) range of interest in the present article, for a fixed d_p / d_t, and for constant thermophysical properties, Eq. 12 may be well approximated by the linear dependence of $Nu_{w,HE}$ on Re_p:

$$Nu_{w,HE} = 0.23Re_p + 27.9 \quad (13)$$

The correlated $U_{w,HE}$ values were in the range of $\approx 0.15 - 0.25$ kJ / (m^2 s K) for $Re_p = 5 - 100$ used in the simulations. These values are similar to those estimated from an overall approximate heat balance using the experimental data, yielding values in the range of $U_{w,HE} \approx 0.06 - 0.18$ kJ / (m^2 s K) for $Re_p = 5 - 20$.

Wall Heat Transfer and Axial Heat Dispersion.

The wall heat transfer ($U_{w,HL}$) and the effective axial heat dispersion coefficients (k_{ax}) were obtained by fitting an approximate analytical solution of the temperature distribution along the reactor to the experimental data using a least squares analysis. To express the temperature profile analytically, it was assumed that at steady state most of the reactions and the heat transfer between the Ox and SR compartments take place immediately at the reactor entrance (the experimentally observed hot spot is indeed located very close to the reactor entrance,[23,24] as it is expected for low gas velocities[6]) and further temperature drop is mainly due to the heat losses through the reactor wall. These assumptions imply that MOx occurs immediately. For this domain the steady state enthalpy balance for the Ox compartment accounts for axial thermal dispersion, convection and heat losses:

$$0 = k_{ax}^{Ox}\frac{d^2T^{Ox}}{dz^2} - \varepsilon^{Ox}(v\rho C_p)_g^{Ox}\frac{dT^{Ox}}{\partial z} - a_{v,HL}^{Ox}U_{w,HL}(T^{Ox} - T_a) \quad (14)$$

$$T^{Ox}\big|_{z=0} = T_{max}^{Ox}; \qquad \left.\frac{dT^{Ox}}{dz}\right|_{z=L} = 0 \quad (15)$$

The solution of this (ordinary, second-order) differential equation is

$$T - T_a = (T_{max} - T_a)\frac{m_1 e^{m_1}e^{m_2\xi} - m_2 e^{m_2}e^{m_1\xi}}{m_1 e^{m_1} - m_2 e^{m_2}} \quad (16)$$

$$m_{1,2} = \frac{Pe \pm \sqrt{Pe^2 + 4Pe\overline{U}}}{2}, \quad Pe = \frac{\varepsilon(v\rho C_p)_g L}{k_{ax}}, \quad \overline{U} = \frac{\alpha_{v,HL}U_{w,HL}L}{\varepsilon(v\rho C_p)_g}$$

The parameters $U_{w,HL}$ and k_{ax}^{Ox} were extracted by fitting Eq. 16 to temperature profiles measured in the experiments ($Re_p = 5 - 20$) with three parameters (k_{ax}, $U_{w,HL}$ and T_{max}) using a least squares analysis. T_{max} is an imaginary parameter representing the temperature at the entrance due to the heating by MOx and cooling as a results of MSR; it is not used in the exact numerical model. Individual values of the three parameters were determined for each experiment (total 8 experiments) and then correlated with flow rate. The wall heat transfer coefficient ($U_{w,HL}$) was found to exhibit a power dependence on Re_p, whereas the effective axial heat dispersion coefficient was linearly dependent on Re_p:

$$Nu_{w,HL} = \frac{U_{w,HL}d_p}{k_g} = 0.21Re_p^{0.5} \quad (17)$$

$$\frac{k_{ax}}{k_g} = 32.6Re_p + 54.5 \quad (18)$$

The relatively high k_{ax} / k_g values may be attributed to the additional contribution of the heat conduction along the walls of the SR and Ox compartment tubes (stainless steel, 0.9 and 1.6 mm thick, Table 1). The obtained axial heat dispersion correlation (Eq. 18) was used for both Ox and SR compartments.

Axial Mass Dispersion.

The effective axial mass dispersion coefficient is obtained from the following correlation[32]:

$$D_{ax} = \varepsilon\left(\frac{D_m}{\tau_b} + 0.5d_p v_g\right) \quad (19)$$

The correlated values of D_{ax} were in the range of $\approx 1 \times 10^{-4} - 7.5 \times 10^{-4}$ m^2 / s, for $Re_p = 10 - 100$ used in the simulations.

Numerical solution validation

The model was found to predict well the experimentally measured temperature profiles and the experimental data in general, as it is shown in Figure 2, where SR conversion (f^{SR}), CO yield (Y_{CO}, moles of CO generated per moles of CH_4 reacted in MSR) and outlet membrane hydrogen flux $J_{H_2,out}^{M}$) are plotted versus $4Pe_M^*$, the ratio of methane feed to hydrogen transport capacity (Eq. 20, evaluated at $T = T_{ref} = 650°C$). P_t^{SR} is the total pressure in the SR compartment. The agreement was good for the two different membranes tested.

$$Pe_M = \frac{y_{mf}F_{tf}}{S^M A_{H_2}\sqrt{P_t^{SR}}\exp[-E_{H_2}/(R_g T)]} \quad (20)$$

Figure 2c represents the hydrogen production in terms of the total hydrogen recovery (HR) and the corresponding fuel cell electrical power output (P):

$$HR = \frac{F_{H_2}^{M}}{F_{mf}^{SR} + F_{mf}^{Ox}} \quad (21)$$

$$P = \eta^{FC}\Delta G^{FC}F_{H_2,out}^{M} = \eta^{FC}\Delta G^{FC}(J_{H_2,out}^{M}S^{M})/(N_c) \quad (22)$$

In Eq. 22, a fuel cell efficiency of $\eta^{FC} = 0.6$ is assumed; $\Delta G^{FC} = 237$ kJ / mol is the Gibbs free energy for fuel cell hydrogen oxidation reaction and N_c is a conversion factor from volumetric to molar flux.

The total hydrogen recovery, moles of hydrogen separated by the membrane per total moles of methane fed, defines in fact the reactor efficiency. The theoretical thermodynamic maximal HR value is estimated from $(-\Delta H)^{Ox}\ F_{mf}^{Ox} = -(-\Delta H)^{SR}\ F_{mf}^{SR}$ and $F_{H_2}^{M} = 4F_{mf}^{SR}$, i.e., assuming complete SR

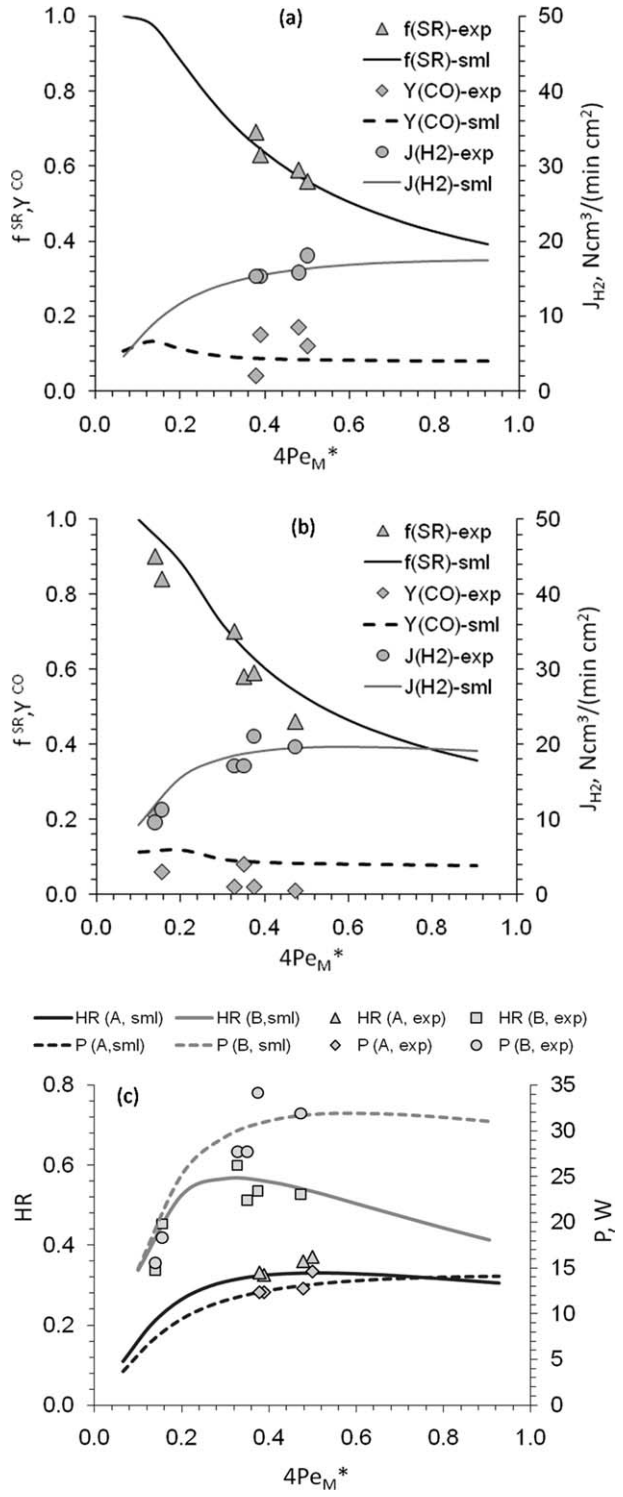

Figure 2. Simulated and experimentally obtained reformer performance plotted versus $4Pe^*_M$, showing SR conversion (f^{SR}), CO selectivity (Y_{CO}), and hydrogen flux ($J^M_{H_2}$): (a) membrane A (Table 2, a^M_v = 5.7 m^{-1}), SV^{SR} = 140–190 h^{-1}; (b) membrane B (Table 2, a^M_v = 11.5 m^{-1}), SV^{SR} = 160–560 h^{-1}; (c) hydrogen recovery (*HR*) and power output (*P*), membranes A and B; parameters: $y^{Ox/SR}_{mf}$ = 0.075/0.3, SV^{Ox} = 1000 h^{-1}.

conversion, no CO formation and adiabatic operation with complete heat recuperation. This corresponds to $HR = 4 / (1+ 165 / 803) = 3.32$, which we set to be equivalent to the reactor efficiency of 1. A less conservative adiabatic efficiency limit defined as above, but accounting for the sensible heat carried by the outlet stream, i.e., $(-\Delta H)^{Ox} F^{Ox}_{mf} = -(-\Delta H)^{SR} F^{SR}_{mf} + C_{pg} (F^{Ox}_{tf} + F^{SR}_{tf})(T_{eff} - T_f)$, yields $HR = 2.7$ (reactor efficiency of ~0.8) for the effluent temperature of T_{eff} = 700°C and the parameters of Figure 2.

Note that:

(i) High SR conversions can be achieved for $4Pe^*_M < 0.2$.

(ii) The performance for the two different membranes are quite similar when it is expressed as a function of Pe_M; as it is shown below (section *Design limits*), there exists an asymptotic solution for very fast kinetics.

(iii) Y_{CO} is much smaller than the values expected for closed-system (without membrane) equilibrium due to the separation of hydrogen and declining temperature along the reactor, as we show elsewhere.[23]

(iv) *HR* is small because of large heat losses,[23,24] and there are maxima in *HR* versus $4Pe^*_M$ plots (it can be particularly seen for membrane B, at $4Pe^*_M \sim 0.3$). Hydrogen recovery from the SR stream (moles of hydrogen separated per moles of methane fed to the SR compartment) was good, varying between 3 and 4 for $4Pe^*_M < 0.2$, when compared with a stoichiometric limit of $4(1 - P^M_t / P^{SR}_t)$. P^{SR}_t and P^M_t are the total pressures in the SR compartment and membrane interior, respectively.

(v) Increasing SR feed (with appropriate increase of Ox feed) will require larger membrane area, but, if the same reactor dimensions are used, the heat loss will be similar and consequently the relative impact of that loss will diminish and *HR* values will be higher.

Model Extension

To demonstrate that the power output of a unit, of the size used in experiments, can be economical the reformer operation is optimized by the following steps: (i) Increasing the membrane area, which allows in turn to increase SR throughput (with some adjustment of Ox flow, as explained below) and consequently to diminish the relative effect of heat loss, and (ii) Reducing the heat loss, as it will be expected in larger units and/or by better thermal insulation. Later we also show that recycling the SR compartment effluent, which includes unreacted methane, to the Ox compartment feed significantly improves the reformer efficiency (we have reported experimental verification of this concept elsewhere[24]).

Figure 3 shows that ~500 W of power is expected from the same unit as that tested experimentally (Figure 2) just by a 20-fold increase in the separation area (nM, number of membranes, parameters of membrane B were used, Table 2), also increasing significantly hydrogen recovery to ~1.2 (compare with an adiabatic thermodynamic limit of ~3.3 with complete heat recuperation and ~2.7 in a normal cocurrent operation mode). Recall that introducing more separation area allows to increase the SR throughput, i.e., SV^{SR}, but it has to be compensated by increasing the flow rate in the Ox compartment, to keep a sufficiently high reactor temperature. To maintain average temperatures similar to those measured in the experiments (~650°C[24]), the Ox feed flow

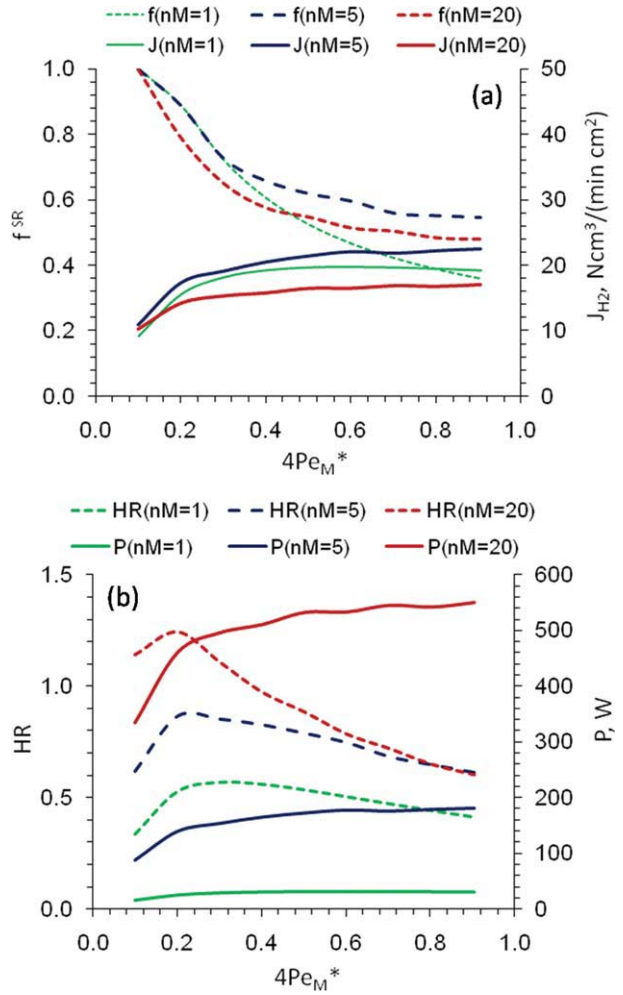

Figure 3. Predicted improved reformer performance, upon adding membrane area (a_v^M = 11.5, 57.6, 230.5 m^1, nM = 1, 5, 20), showing (a) SR conversion (f^{SR}) and hydrogen outlet flux J_{H_2} and (b) hydrogen recovery (HR) and power output (P) versus $4Pe_M^*$, SV^{Ox} =1000, 5000, 10000 h^1, respectively; parameters: y_{mf}^{SR} = 0.33, y_{mf}^{Ox} is defined by Eq. 23.

[Color figure can be viewed in the online issue, which is available at wileyonlinelibrary.com.]

rate was increased from SV^{Ox} = 1000 h^{-1} at nM = 1 to 5000 and 10000 h^{-1} for nM = 5, 20. The Ox compartment methane feed concentrations (y_{mf}^{Ox}) was estimated by the overall energy balance (with $T_{eff}^{Ox} = T_{av}^{Ox}$ = 650°C and assuming $T^{Ox} = T^{SR}$):

$$y_{mf}^{Ox} = \frac{-(-\Delta H)^{SR} F_{mf}^{SR} + (T_{eff}^{Ox} - T_f) C_p (F_{tf}^{SR} + F_{tf}^{Ox}) + S^W U_w (T_{av}^{Ox} - T_a)}{(-\Delta H)^{Ox} F_{tf}^{Ox}} \quad (23)$$

This yielded $y_{mf}^{Ox} \sim 0.04 - 0.07$, and resulted in a spatially averaged simulated SR temperatures in a range of $T_{av}^{SR} \sim$ 560 – 620°C (lower than the target value due to the assumptions made in Eq. 23). Interestingly, quite a similar performance was obtained in terms of f^{SR} and $J_{H_2,out}^M$ versus $4Pe_M^*$ for different separation areas (Figure 3), indicating that this representation can be used for generalization of results: high conversions are obtained for $4Pe_M^* < 0.2$.

An efficiency of $\eta = HR / 3.32 \approx 0.7$ and the power output (P) of 600 W are predicted for the reformer, when the separation area is increased 20-fold and the heat losses are reduced to 1/4 of their value in experiments and the methane utilization is optimized, Figure 4 ($y_{mf}^{Ox} \sim 0.07$, SV^{Ox} = 4000 h^{-1}); η and P are presented as a function of methane utilization (MU), defined as moles of methane fed for Ox per moles of methane fed for SR:

$$MU = \frac{F_{mf}^{Ox}}{F_{mf}^{SR}} \quad (24)$$

Note that there is an optimal η as MU is increased, and it is shifted to lower MU values as the heat losses are reduced. The efficiencies obtained here are very close to the adiabatic efficiency limit for cocurrent operation (~0.8, see section Numerical solution validation). The volumetric power density of the simulated reformer (see dimensions in Table 1), corresponding to 600 W, is 0.96 kW/L.

Design limits

Approximate solutions of the steam reforming conversion, the corresponding hydrogen flux and of the temperature distribution along the reformer are derived below for the asymptotic case of an infinitely fast reaction. This will provide the membrane area design limit; the reformer thermodynamic optimization algorithm is subsequently derived based on this design limit (section *Thermodynamic optimization algorithm*). In the following subsections we consider this kinetic design limits for the SR reactions, and a design criterion that will avoid extinction in the Ox reaction.

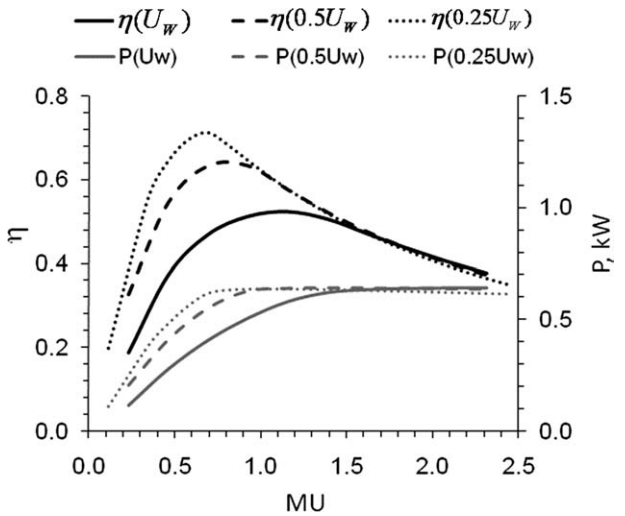

Figure 4. Predicted improved reformer performance for decreased heat loss coefficient from current experimental value (U_W) in terms of efficiency (η) and power output (P) ($y_{mf}^{Ox/SR}$ = 0.07/0.33, a_v^M = 230.5 m^1, SV^{SR} = 4000 h^1).

Steam reforming conversion and hydrogen separation: the fast reaction case

Methane SR conversion (f^{SR}) in a membrane reformer depends mainly on the hydrogen transport rate that shifts the SR equilibrium, and on the reformer temperature that affects SR kinetics, SR equilibrium, and H_2 separation. Here, an analytical approach, based on the asymptote of fast reaction, is derived to provide analytical expressions for calculating f^{SR} as a function of equilibrium parameters and membrane Peclet number (Pe_M).

At steady isothermal conditions, while neglecting mass dispersion and assuming no net CO formation (SR is represented solely by Eq. 3), Eq. 6 is reduced to the following SR compartment mass balance ($R_{SR} \equiv R_3$, $k_{SR} \equiv k_3$):

$$\varepsilon\rho_g v_g \frac{dy_i}{dz} = \alpha_{iSR}\rho_c(1-\varepsilon)R_{SR} - a_{vM}^{SR}A_i \exp\left(-\frac{E_{H_2}}{R_g T}\right)\Delta(\sqrt{p_i}) \tag{25}$$

This can be reduced to two equations (at a given temperature) describing the distribution of CH_4 and H_2 along the SR compartment ($f = (y_{mf}^{SR} - y_m^{SR}) / y_{mf}^{SR}$, $z = \xi L$):

$$\frac{df}{d\xi} = Da_{SR}\mathrm{K} \tag{26}$$

$$\frac{1}{y_{mf}}\frac{dy_{H_2}}{d\xi} = 4Da_{SR}\mathrm{K} - \frac{1}{Pe_M}\left(\sqrt{y_{H_2}} - \Phi\right), \quad \Phi = \sqrt{\frac{P_t^M}{P_t^{SR}}} \tag{27}$$

$$Da_{SR} = \frac{\rho_c(1-\varepsilon)k_{SR}V}{y_{mf}F_{tf}\sqrt{P_t^{SR}}}, \quad K = \frac{\sqrt{P_t^{SR}}}{p_{H_2}^{3.5}\Gamma^2}\left(p_{CH_4}p_{H_2O}^2 - \frac{p_{H_2}^4 p_{CO_2}}{K_{eq,SR}}\right) \tag{28}$$

Combining Eqs. 26 and 27 yields:

$$\frac{d(4f - y_{H_2}/y_{mf})}{d\xi} = \frac{1}{Pe_M}\left(\sqrt{y_{H_2}} - \Phi\right) \tag{29}$$

In the limit of an infinitely fast SR reaction, the equilibrium is assumed to be instantaneously established everywhere, while the reacting mixture composition varies only in response to hydrogen transport.[33,34] Then, the SR conversion can be represented by the SR equilibrium ($f \equiv f_e$, derivation is provided in the Appendix, Eqs. A1–A3):

$$\frac{4(1-f)^3(1-y_{H_2})^3}{(3-2f)^3} - \frac{1}{K'}\frac{y_{H_2}^4 f(1-y_{H_2})}{(3-2f)} = 0, \quad K' = \frac{K_{eq,SR}}{(P_t^{SR})^2} \tag{30}$$

Although Eqs. 29 and 30 can be solved numerically, an approximate analytical solution based on correlating equilibrium conversion (f_e) with equilibrium H_2 fraction (y_{H_2}) using Eq. 30 is derived here. Figure 5 shows that for $f_e > 0.1$, f_e can be well approximated as $f = ay^2 + by + c$ ($y \equiv y_{H_2}$) for various temperatures. Recall that $K_{eq,SR} \equiv K_{eq,SR}(T)$, so that $a \equiv a(T, P_t^{SR})$ etc.

Substitution of $f = ay^2 + by + c$ into Eq. 29 with subsequent integration yields quite a simple analytical expression, Eq. 31 (derivation is provided in the Appendix, Eqs. A4–A6). The integration constant is found using the inlet condition $y(0) = y_e$ (y_e is the equilibrium value for a closed system). It is also assumed that $\Phi \to 0$, i.e., $P_t^{SR} \gg P_t^M$ (high SR operation pressure or/and applying vacuum in the membrane interior).

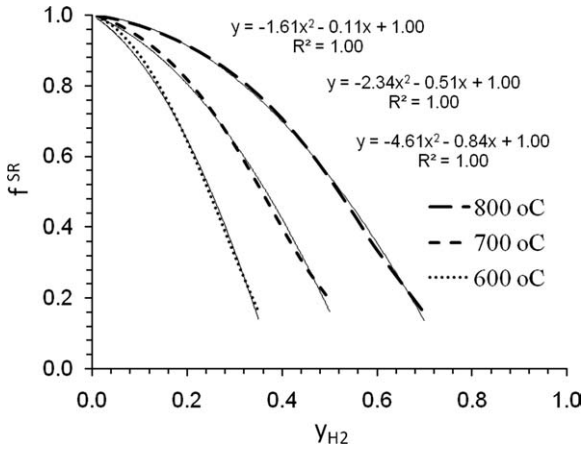

Figure 5. Equilibrium SR conversion (f^{SR}) versus H_2 mol fraction y_{H_2} plots, (from Eq. 30) at different temperatures, and their parabolic function fit; $P_t^{SR} = 10$ bar.

$$\frac{8a}{3}(y^{3/2} - y_e^{3/2}) + (4b - 1/y_{mf})(\sqrt{y} - \sqrt{y_e}) = \frac{\xi}{2Pe_M}, \quad y \equiv y_{H_2} \tag{31}$$

Equation 31 has a form of a cubic polynomial in terms of a new variable $x = \sqrt{y}$, and the solution can be written explicitly (Cardano's method, see the Appendix, Eqs. A7–A9), providing an explicit analytical expression for $y_{H_2}(\xi)$:

$$y_{H_2} = \left(u - \frac{\bar{b}}{3u}\right)^2, \quad u = \sqrt[3]{-\frac{\bar{c}}{2} \pm \sqrt{\frac{\bar{c}^2}{4} + \frac{\bar{b}^3}{27}}} \tag{32}$$

$$\bar{b} = \frac{3(4b - 1/y_{mf}^{SR})}{8a},$$

$$\bar{c} = \left(-y_e^{3/2} - \frac{3(4b - 1/y_{mf}^{SR})}{8a}\sqrt{y_e} - \frac{3\xi}{16aPe_M}\right)$$

Figure 6a plots the reformer outlet SR conversion (f^{SR}) calculated by Eq. 30 (f corresponds to the outlet H_2 molar fraction $y_{H_2}(1)$, Eq. 32) shown as triangles. It is also shown that the temperature dependence of f^{SR} can be well fitted with two parameters by

$$f^{SR} = \frac{\alpha^{SR}\exp(-\beta^{SR}/T)}{1 + \alpha^{SR}\exp(-\beta^{SR}/T)} \tag{33}$$

The transport-limited conversion (f^{SR}, calculated by Eqs. 30, 32, Figure 6b) increases with T due to shifting equilibrium and with Pe_M^* (calculated by Eq. 20 with $T_{ref} = 650°C$ and $P_t^M = 0.1$ bar). This figure shows the minimal temperature required to achieve the desired conversion, provided the catalyst is sufficiently active. As expected, this $f^{SR}(T)$ curves converges at low Pe_M^* to the SR membrane equilibrium

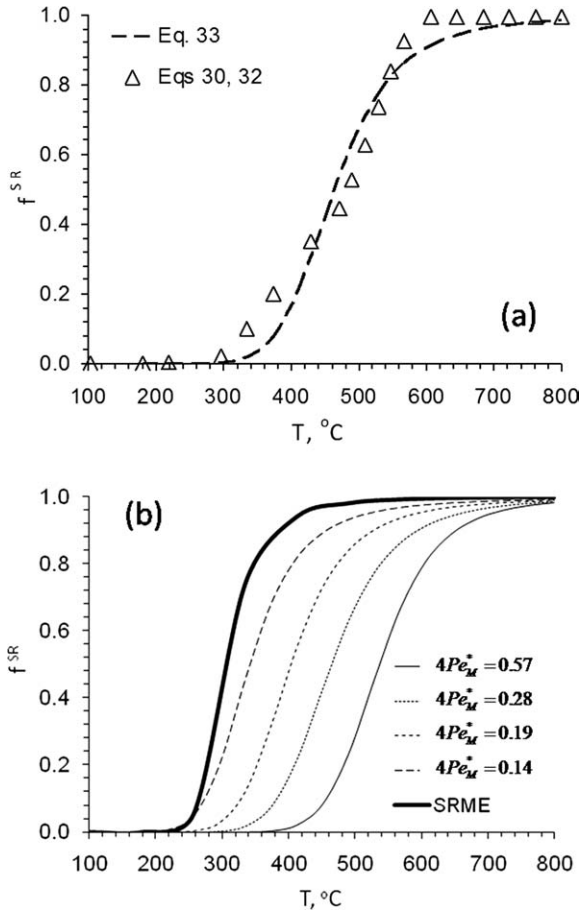

Figure 6. Limiting SR conversion (f^{SR}) for fast reactions as a function of temperature calculated by Eqs. 30, 32 for (a) $4Pe^*_M = 0.28$ (showing also its parametric fit by Eq. 33), and (b) various Pe^*_M (the SR membrane equilibrium conversion, SRME, is also shown).

conversion (calculated by Eq. 30, while assuming complete hydrogen separation, i.e., $y_{H_2}P_t^{SR} = P_t^M$). The equilibrium is nearly approached for $4Pe^*_M < 0.2$.

The overall hydrogen flux, corresponding to the fast reaction asymptote, can be computed by integration of the local flux (Sievert's law) along the reformer, under the assumptions above:

$$J^M_{H_2,out} = A_{H_2}\exp\left(\frac{-E_{H_2}}{R_g T_{av}}\right)\sqrt{P_t^{SR}}\int_0^1 (\sqrt{y(\xi)} - \Phi)d\xi \quad (34)$$

$$T_{av} = \int_0^1 T(\xi)d\xi \quad (34a)$$

Typical $y(\xi)$ spatial distribution (Eq. 32) and the corresponding cumulative hydrogen flux ($J_{H_2}(\xi)$, Eq. 34) are presented in Figure 7. The outlet hydrogen flux ($J^M_{H_2,out}$) calculated by Eqs. 32, 34 for $0.14 < 4Pe^*_M < 0.57$ shows a limiting value at high T (Figure 8a); $J^M_{H_2,out}$ can be well correlated with two parameters (in similarity to f^{SR}) by

$$J^M_{H_2,out} = \frac{J^M_{H_2,max}\alpha^M\exp(-\beta^M/T)}{1+\alpha^M\exp(-\beta^M/T)}, \quad J^M_{H_2,max} = 4F^{SR}_{mf}/S^M \quad (35)$$

Note that the actual hydrogen output flow rate, which in turn determines the fuel cell stack power output, is a product of the hydrogen outlet flux and the separation area. Plotting the power output (P, Eq. 22) at a constant methane SR feed flow rate of 2.4 NL/min (a value required for ~1 kW fuel cell power output) shows that P depends crucially on Pe_M (Figure 8b), i.e., on the separation area, particularly for relatively low temperatures. For reasons of membrane stability (800°C is about an upper limit for Pd-Ag membranes) and thermal efficiency (the higher the reformer temperature the higher is the heat loss) it is preferable to use more separation area and to operate the reformer at relatively low temperatures. This should be weighted in against the membrane cost. Clearly, the temperature also should be sufficiently high to provide reasonable activity, while the reactor volume should be sufficiently small. The methane SR feed flow rate for Figure 8 follows from

$$F^{SR}_{mf} = \frac{F^M_{H_2,out}}{4\delta(1-P_t^M/P_t^{SR})} = \frac{P}{4\delta(1-P_t^M/P_t^{SR})\eta^{FC}\Delta G^{FC}} \quad (36)$$

Equation 36 accounts for incomplete SR and WGS conversions ($\delta = 0.95$ is assumed), while the factor $(1 - P_t^M/P_t^{SR})$ accounts for incomplete hydrogen separation.

Reformer temperature

The reformer temperature should be known to calculate the SR conversion and hydrogen production rate (Eqs. 30–35). The approximate analytical solution for the temperature distribution was derived in section *Transport coefficients*, Eqs. 16–18. The reformer overall enthalpy balance accounts for the heat generated by MOx, consumed by MSR, and removed with the effluent streams, and the heat losses to the environment:

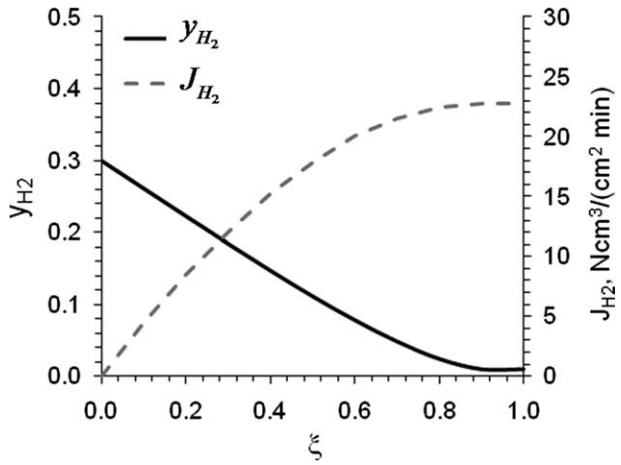

Figure 7. Spatial variation of hydrogen molar fraction y_{H_2} and membrane flux J_{H_2} along reformer length (ξ).

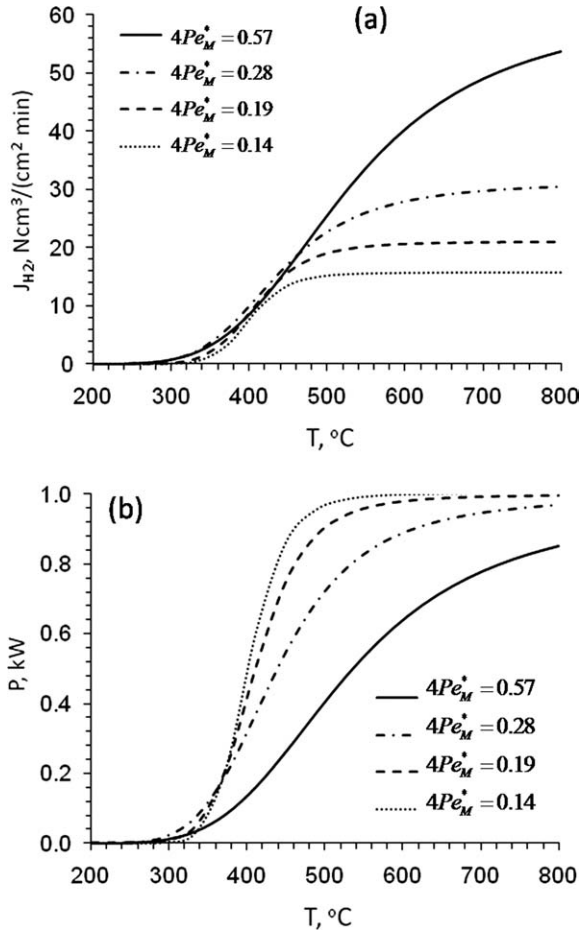

Figure 8. Limiting hydrogen production rate for various Pe_M^* as a function of temperature: (a) hydrogen outlet membrane flux $J^M_{H_2,out}$ calculated by Eqs. 32, 34; (b) corresponding power output (P, Eq. 22), calculated for SR methane feed flow rate of Q^{SR}_{mf} = 2.4 NL/min.

$$\sum(-\Delta H^k)y^k_{mf}F^k_{tf}f^k - (T_{eff}-T_f)C_{pg}\sum F^k_{tf} - S^{Ox}U_w\int_0^1 (T(\xi)-T_a)d\xi = 0 \quad (37)$$

$$k \equiv Ox, SR$$

The temperature distribution is then computed by iterative solution of Eqs. 16 and 37. (i) T_{max} is first guessed, and the temperature distribution $T(\xi)$ and the effluent temperature T_{eff} are calculated by Eq. 16. Equations 17 and 18 provide correlations for the heat transfer parameters; (ii) T_{max} (the initial guess), $T(\xi)$ and T_{eff} are then substituted into Eq. 37. The Ox and SR conversions ($f^{Ox}(T_{max})$ and $f^{SR}(T_{eff})$, Eqs. 10a and 33) are calculated at the maximum and effluent temperature, respectively; (iii) If Eq. 37 is not satisfied, T_{max} is corrected again and so on, until a set of T_{max}, T_{eff}, and $T(\xi)$ that satisfies Eq. 37 is found.

SR kinetic limits

Two main assumptions have been made in the analytical solution of the model: (i) infinitely fast SR reaction and (ii) infinite heat transfer between the SR and Ox compartments. The first assumption is valid when $Da_{SR} \gg 1$ (i.e., the initial rate of the SR reaction is higher than the methane feed rate, see Eq. 28 for definition). The following condition should be also satisfied (reaction rate is higher than separation rate):

$$4Pe_M Da_{SR} = \frac{4A_{SR}\exp\left[-E_{SR}/(R_gT)\right]\rho_c(1-\varepsilon)V}{P_t^{SR}S^M A_{H_2}\exp\left[-E_{H_2}/(R_gT)\right]} \gg 1 \quad (38)$$

Note that for $4Pe_M \sim 1$, which is a practical range, the two limits are identical. Plotting this term versus T for various membrane areas (Figure 9, 150–600 cm^2) shows that the analytical solution is restricted to $T > 550$°C and to $T > 650$°C for 500 g (black lines) and 50 g (grey lines) of Ni/Al_2O_3 (16.5 wt % NiO) catalyst, respectively, and methane feed flow rate required for a ~1 kW unit. Higher operation temperatures allow reducing both catalyst amount and membrane area, but also may harm membrane durability. A search for a better catalyst is necessary to obey these conditions. Recent reports suggest that SR reactions can well proceed on Ru-based catalyst at ~500°C in a membrane reactor.[9] Experiments[23,24] and simulations showed that temperature intercompartment differences are indeed small, supporting the assumption (ii); but significant gradients may arise at the reactor entrance for high flow rates. As the analytical approach does not account for these gradients, it is expected to overestimate the temperature near to the reactor entrance.

Ox kinetic limits

In a packed bed catalyzing oxidation reaction (e.g., MOx), hot spots, which move due to convection and conduction, are expected to occur. If this front (in adiabatic systems) or

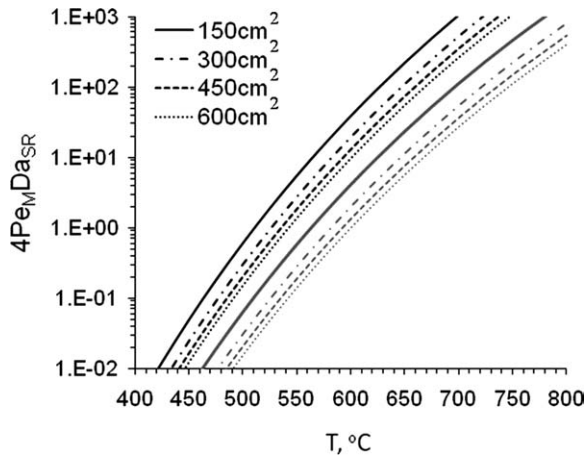

Figure 9. Dimensionless reaction-to-separation rates ratio ($4Pe_MDa_{SR}$) as a function of temperature for different separation areas and SR catalyst amounts (black lines = 500 g, grey lines = 50 g), P_t^{SR} = 10 bar, membrane B.

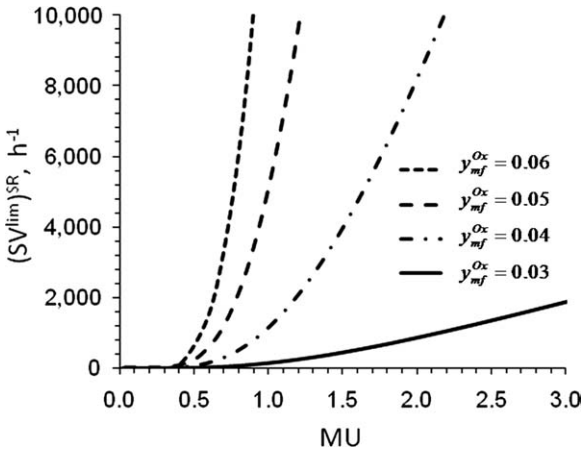

Figure 10. Limiting SR gas space velocity $(SV^{SR})^{lim} = (v_g^{Ox})^{lim}/L$, that will sustain a front within the system, as a function of methane utilization (MU) for different CH_4 Ox feed concentrations (y_{mf}^{Ox}), calculated by Eqs. 39, 40 for a 1 kW unit (Table 3, $Q_{mf}^{SR} = 2.4$ NL/min, $y_{mf}^{Ox} = 0.33$).

pulse (in nonadiabatic systems with heat losses) leaves the system, the conversion drops to zero. The reactor limiting throughput is determined by the conditions that induce downstream propagating hotspots. A design criterion for this limit, for a spatially separated reactive coupling unit (e.g., MSR + MOx), has been reported elsewhere[6]; it provides an analytical expression for the limiting average feed velocity ($\overline{v_g^{lim}}$):

$$\overline{v_g^{lim}} = \frac{T_p\sqrt{\alpha}}{\lambda\sqrt{T_f\overline{\Delta T}}}\sqrt{\frac{\rho_s}{\varepsilon\rho_g C_{pg}}\frac{\overline{k_{ax}}A_{Ox}}{\gamma}\exp\left(-\frac{\gamma T_f}{T_p}\right)} \quad (39)$$

$$\overline{v_g^{lim}} = (v_g^{lim})^{SR}(1-\alpha) + (v_g^{lim})^{Ox}\alpha, \quad \overline{k_{ax}} = k_{ax}^{SR}(1-\alpha) + k_{ax}^{Ox}\alpha,$$

$$\alpha = \frac{A_{cs}^{Ox}}{A_{cs}^{SR} + A_{cs}^{Ox}}$$

$$\gamma = \frac{E_{Ox}}{R_g T_f}, \quad T_p = T_f + \lambda\overline{\Delta T}, \quad \lambda = \frac{y_{mf}^{SR} MU}{y_{mf}^{Ox} + y_{mf}^{SR} MU},$$

$$\overline{\Delta T} = \frac{(-\overline{\Delta H})y_{mf}^{Ox}}{C_{pg}}$$

Equation 39 evaluates axial conduction and oxidative heat generation that induce upstream hot spot propagation (right side of Eq. 39), against convection that pushes the hot spot downstream (left side of Eq. 39). The effects of the endothermic reaction are accounted for via geometry and methane utilization factors (α, λ) and via enthalpy effects ($(-\overline{\Delta H})$[6]). Although Eq. 39 was developed for adiabatic systems, we modify it for nonadiabatic systems. As the main effect of heat losses on thermal spot dynamics will be through the peak temperature, we estimate $\overline{\Delta T}$ to account for the heat losses as follows:

$$\overline{\Delta T} \approx \frac{(-\overline{\Delta H})y_{mf}^{Ox}/C_{pg}}{1 + S^w U_w/(F_{tf}^{Ox} C_{pg})} \quad (40)$$

Figure 10 presents the limiting SR throughput ($(SV^{lim})^{SR} = (v_g^{lim})^{SR} / L$) calculated for a 1 kW unit and various Ox methane feed concentrations (y_{mf}^{Ox}), showing a steep performance drop for small *MU*. Operation is limited to the domain below the $(SV^{lim})^{SR}$ versus *MU* curve (for a given y_{mf}^{Ox}), while the right boundary is limited by *MU*, which should be held below 1; using $MU > 1$ results in inefficient operation and overheating (as it is demonstrated in the following section). It can be also seen that using relatively high methane feed concentrations is preferable and it should be at least higher than 0.04. The limiting throughput calculations were in a good agreement with the analytical prediction (see next section).

Thermodynamic optimization algorithm

The analytical approach described in the previous section approximates the reformer temperature distribution, SR conversion and hydrogen outlet flux for a given set of parameters. We use this approach now for predicting and optimizing the reformer performance. Note that the optimization is based on thermodynamics and equilibrium data and does not account for kinetic limitations; the kinetics is considered only through the restriction of sufficiently high $4Pe_M Da_{SR}$ for the SR reaction and the condition avoiding down-stream moving fronts (as it is described in previous section) for the oxidation reaction.

In the process we set a desired reformer power output (*P*, Eq. 22) and optimize reformer efficiency (η). To calculate $\eta = HR_{anl} / HR_{max}$ ($HR_{max} = 4/(1 + 165 / 803) = 3.32$, section *Numerical solution validation*), hydrogen recovery (*HR*) is first estimated, based on the overall enthalpy balance, as a function of the operation parameters:

$$f^{Ox}(-\Delta H)^{Ox}F_{mf}^{Ox} = -f^{SR}(-\Delta H)^{SR}F_{mf}^{SR} + \Delta T_r C_p(F_{tf}^{SR} + F_{tf}^{Ox}) + S^W U_w \Delta T_w \quad (41)$$

$$\Delta T_r = T_{eff} - T_f, \quad \Delta T_w = T_{av} - T_a, \quad T_{av} = \int_0^1 T(\xi)d\xi$$

$$HR_{anl} = \frac{4f^{SR}F_{mf}^{SR}}{F_{mf}^{SR} + F_{mf}^{Ox}} = \frac{4f^{SR}}{1 - \frac{f^{SR}\Delta H^{SR}}{f^{Ox}\Delta H^{Ox}} + \frac{\Delta T_r C_p}{f^{Ox}(-\Delta H^{Ox})}\left(\frac{MU}{y_{mf}^{Ox}} + \frac{1}{y_{mf}^{SR}}\right) + \frac{MU}{y_{mf}^{Ox} f^{Ox}(-\Delta H)^{Ox}}\frac{S^W U_w \Delta T_w}{F_{tf}^{Ox}}} \quad (42)$$

Optimization algorithm

The following algorithm computes the reformer efficiency (η) and the power output (*P*) of a polymer electrolyte membrane fuel cell (PEMFC) stack fueled by hydrogen generated by the reformer.

(i) For a desired power output (*P*), the required methane SR inlet flow rate (F_{mf}^{SR}) is calculated by Eq. 36.

(ii) For F_{mf}^{SR} calculated in (i), the expected power output (*P*) is mapped, for infinitely fast reaction, in a domain of operation temperature and membrane area by Eqs. 32, 34, and 22. Both parameters affect equilibrium conversion and usually there is a tradeoff between the two. The required membrane area is then evaluated considering the desired operation temperature and membrane cost.

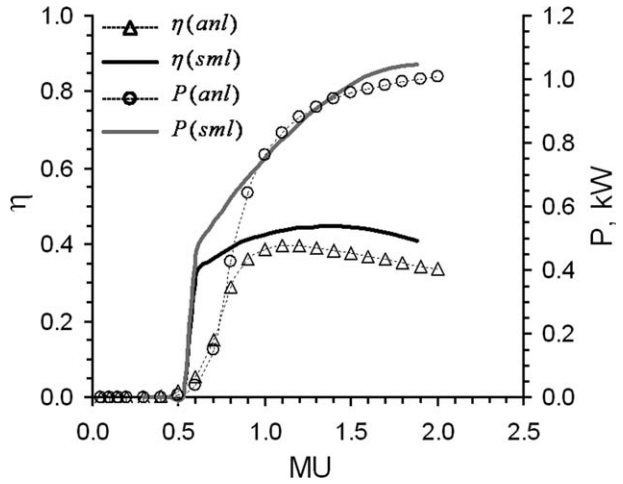

Figure 11. Analytical model prediction and simulations of the 1 kW unit (Table 3) in terms of efficiency (η) and power output (P) as a function of methane utilization (MU); Q_{mf}^{SR} = 2.4 NL/min, S^{M} = 450 cm^2, a_v^M = 46 m^1, y_{mf}^{Ox} = 0.05.

(iii) The reformer geometry is defined considering the separation area defined in (ii), i.e., providing enough space for the membranes, minimizing pressure drop through the packed beds etc. The catalyst loading is selected to provide sufficiently high SR initial reaction rate, i.e., to satisfy $Da_{SR} \gg 1$ and $4Pe_M\, Da_{SR} > 1$ (see section *SR kinetic limits*).

(iv) The reformer efficiency (η) is estimated by Eq. 42, with Eqs. 10a, 33 (conversions) and 16, 37 (temperature) and the power output (P) is computed by Eqs. 35, 22 (using previously defined temperature), for F_{mf}^{SR} defined in (i) and the reformer geometry defined in (ii, iii). Then, η and P are plotted in the methane Ox feed concentration versus methane utilization (y_{mf}^{Ox} versus MU) operation window. Recall that conversions and hydrogen flux are temperature-dependent; therefore an iterative procedure is required (as it is described in section *Reformer temperature*).

Analytical solution validation

A typical example of good agreement between the analytical approximated solution (open symbols) and the exact numerical model solution (solid lines), both expressed in terms of the reformer efficiency (η) and power output (P) versus methane utilization (MU) is shown in Figure 11. Recall, that many assumptions have been made in derivation of the analytical solution. Yet, it shows an acceptable agreement with the exact model. However, the analytical solution differs significantly at low MU values, where a transition from the extinguished state (insufficient methane Ox supply) to the ignited states occurs. For most of the MU range, the agreement is good, therefore the analytical solution may be used at least for preliminary estimation of the operation window.

The analytical approximation also provides a good estimation for the experimental data, Figure 12, where the results are presented in terms of the reactor efficiency (η) and power output (P) versus the membrane Peclet number ($4Pe_M^*$, Eq. 20, evaluated at T = 650°C). The analytical solution predicts well the experimental points, confirming that it can be used for estimation of the reactor performance.

1 kW unit optimization

In this section, an example optimization performed for a 1 kW unit is presented. After (i) the required methane SR feed flow rate is calculated, (ii) the power output is estimated as a function of temperature and membrane area, Figure 13. A membrane area of more than 450 cm^2 and the reformer temperature higher than 600°C are required in the case of very fast reactions, to achieve desired equilibrium conversion. For Ni catalysts, high initial SR rate ($Da_{SR} \gg 1$) can be achieved for $T > 500$°C, and thus temperature is not a limiting factor.

Next, the separation area is selected; the selection is mainly based on the membrane thermal durability. The higher the temperature that the membrane can withstand; the lower the required separation area is. Here, it is assumed that the membrane can be operated at 700°C, selecting the membrane area of 450 cm^2 as a design parameter; the reformer dimensions are subsequently defined based on the considerations described in step (iii) above. Table 3 lists the dimensions of the reformer (with 22 hydrogen separation membranes) designed for fueling 1 kW PEMFC stack, $a_v^M = S^M / V^{SR}$.

The final step in the optimization procedure is mapping and optimizing the expected reformer power output and efficiency in the parameters domain, using the membrane area, catalyst loading and reformer dimensions determined before. As SR methane feed flow rate (F_{mf}^{SR}) is defined by the required power output and conversion considerations (step (i), Eq. 36) and the SR methane feed concentration (y_{mf}^{SR}) cannot be significantly varied (0.33 is a stoichiometric maximum, while lower concentrations will lead to a dilution of the reactive stream and less efficient hydrogen separation[23]). The two key design parameters remaining for optimization

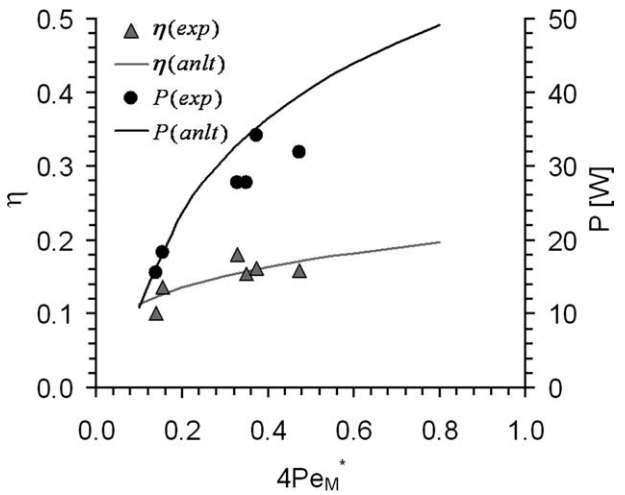

Figure 12. Reformer performance (dimensions listed in Tables 1, 2; membrane B) calculated by analytical model when compared to performance measured in the experiments; a_v^M = 11.5 m^1, $y_{mf}^{Ox/SR}$ = 0.075/0.3, SV^{Ox} = 1000 h^1.

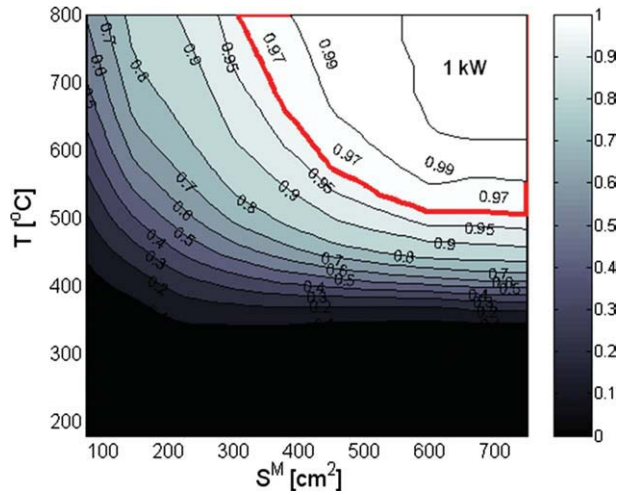

Figure 13. Expected FC stack power output as a function of T and S^M (membrane B); target: 1 kW; Q_{mf}^{SR} = 2.4 NL/min, P_t^{SR} = 10 bar, P_t^M = 0.1 bar.

[Color figure can be viewed in the online issue, which is available at wileyonlinelibrary.com.]

are the Ox methane feed flow rate (or methane utilization, MU) and methane Ox feed concentration (y_{mf}^{Ox}).

Figures 14a–c present the reformer power output and efficiency in a y_{mf}^{Ox} versus MU domain and the corresponding reformer average temperature (T_{av}, defined as in Eq. 34a). The desired power output can be obtained in a relatively wide range, but the reformer efficiency is optimal in a relatively narrow window; the maximum efficiency of $\eta \approx 0.55$ is achieved for $y_{mf}^{Ox} \geq 0.07$ and $0.4 \leq MU \leq 0.7$. Low (practically zero) power output and efficiency are expected for low MU values due to insufficient energy supply from the Ox compartment, leading to reformer temperatures, that are too low to activate SR reactions and H_2 separation, Figure 14c. The efficiency drop for high MU is due to inefficient methane utilization that can also lead to reformer overheating for high methane concentrations, Figure 14c. Interestingly, the operation domain boundaries predicted by the analytical solution is in a relatively good agreement with those predicted by the dynamic model analytical solution, limiting the operation window for $MU > 0.5$ and $y_{mf}^{Ox} > 0.04$ (Eqs. 39, 40, Figure 10).

The thermodynamic optimization showed that there is an optimal MU value and that high efficiency is in general favorable by using high y_{mf}^{Ox} that results in decreasing inlet Ox flow rates and, therefore, lower enthalpy required to heat it up. The detailed parametric study performed both by the thermodynamic calculations and simulations showed that the efficiency can be further improved up to $\eta \approx 0.8$ by providing more separation area and lowering heat losses. Figure 15 shows the simulated performance of the optimized 1 kW unit in terms of P and η; $y_{mf}^{Ox} = 0.075$ was used, the

Table 3. Dimensions of the Reformer Designed for Fueling 1 kW FC Stack

D^M (cm)	L^M (cm)	S^M (cm^2)	D^{SR} (cm)	D^{Ox} (cm)	L^{Ox} (cm)	α_v^M (m^{-1})
0.32	20.3	450	6.4	8.9	30.2	47

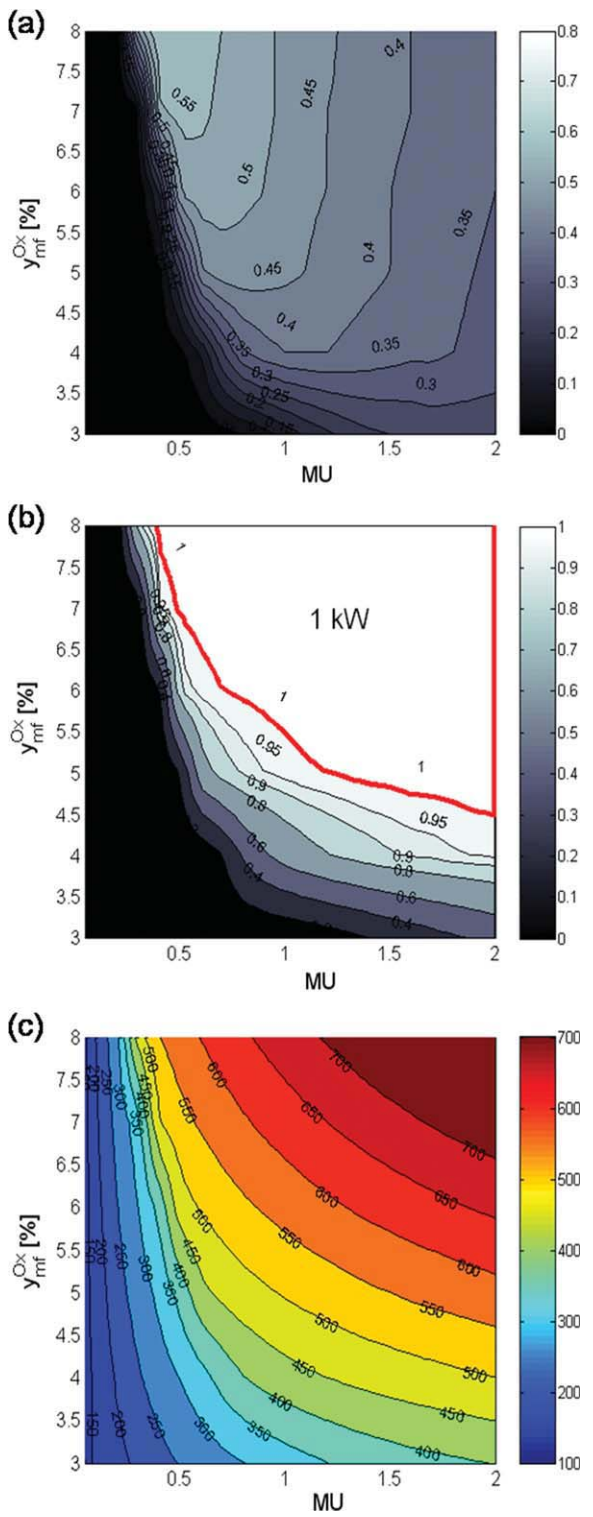

Figure 14. Reformer performance predicted by analytical approximation, 1 kW unit: (a) efficiency (η), (b) power output (P) and average temperature (T_{av}). Q_{mf}^{SR} = 2.4 NL/min, $P_t^{SR/M}$ = 1/0.1 MPa, $4Pe_M^*$ = 0.2, dimensions listed in Table 3.

[Color figure can be viewed in the online issue, which is available at wileyonlinelibrary.com.]

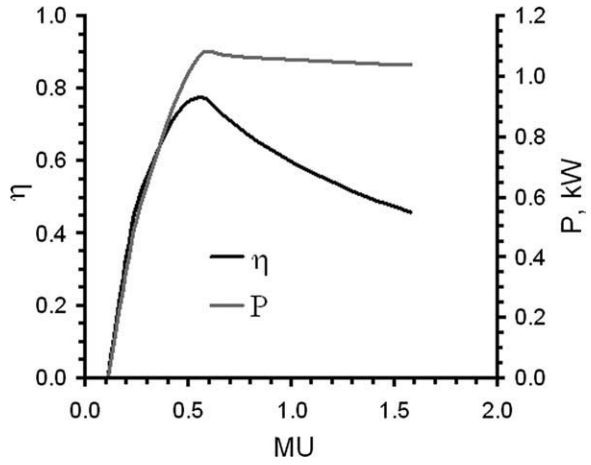

Figure 15. Optimized 1 kW unit, $y_{mf}^{Ox} = 0.075$, $S^{M} = 675$ cm^2, 0.5 U_w; other parameters as in Figure 14.

separation area was increased to 675 cm^2, the heat losses were reduced by 50%. The optimum for η is at $MU \approx 0.6$, where P also achieves its maximal value.

Recycle

To improve the reformer efficiency, SR effluent stream that contains various combustible components, i.e., unreacted methane, unseparated hydrogen, and carbon monoxide, can be recycled to the Ox compartment to provide additional enthalpy. This approach assures (i) higher reformer temperatures, (ii) complete overall methane conversion, (iii) utilization of effluent gases, which are polluted to atmosphere during the normal operation, and, therefore, (iv) no carbon monoxide pollution.

Although the same optimization algorithm is used for calculating the reformer performance with recycle, the equations for the reformer efficiency and temperature rise are modified to account for the recycle. Enthalpy balance is rewritten as follows:

$$f^{Ox}(-\Delta H)^{Ox}[F_{mf}^{Ox} + (1-f^{SR})F_{mf}^{SR}] = f^{Ox}(-\Delta H)^{Ox}RF_{mf}^{Ox}$$

$$MU \equiv \frac{F_{mf}^{Ox}}{F_{mf}^{SR}}, R = \left[1 + \frac{(1-f^{SR})}{MU}\right]$$

$$f^{Ox}(-\Delta H)^{Ox}RF_{mf}^{Ox} = -f^{SR}(-\Delta H)^{SR}F_{mf}^{SR} + \Delta T_r C_p(F_{tf}^{SR} + F_{tf}^{Ox}) + S^{W}U_w\Delta T_w \quad (43)$$

Therefore, to account for recycle, $(-\Delta H)^{Ox}$ is simply multiplied by R in all the calculations. Equation 43 does not account for H_2 and CO in the SR effluent stream, as for efficient H_2 separation (by applying $P_t^M = 0.1$ bar and providing sufficient separation area) the majority of H_2 is separated and most of CO is converted to CO_2 (as it is also supported by the experiments, Figure 2). On the other hand, in U_w calculations we accounted for higher feed flow rates in the Ox compartment, which are the result of the SR effluent addition to the Ox feed. It can be clearly seen from the definition of R that recycling is effective only for small SR conversions and methane utilization ratios. Figures 16a–c present the results of the calculations performed for recycle operation (1 kW target PEMFC stack power output). The operation window is significantly widened and much higher efficiencies can be obtained, while using the recycle operation mode.

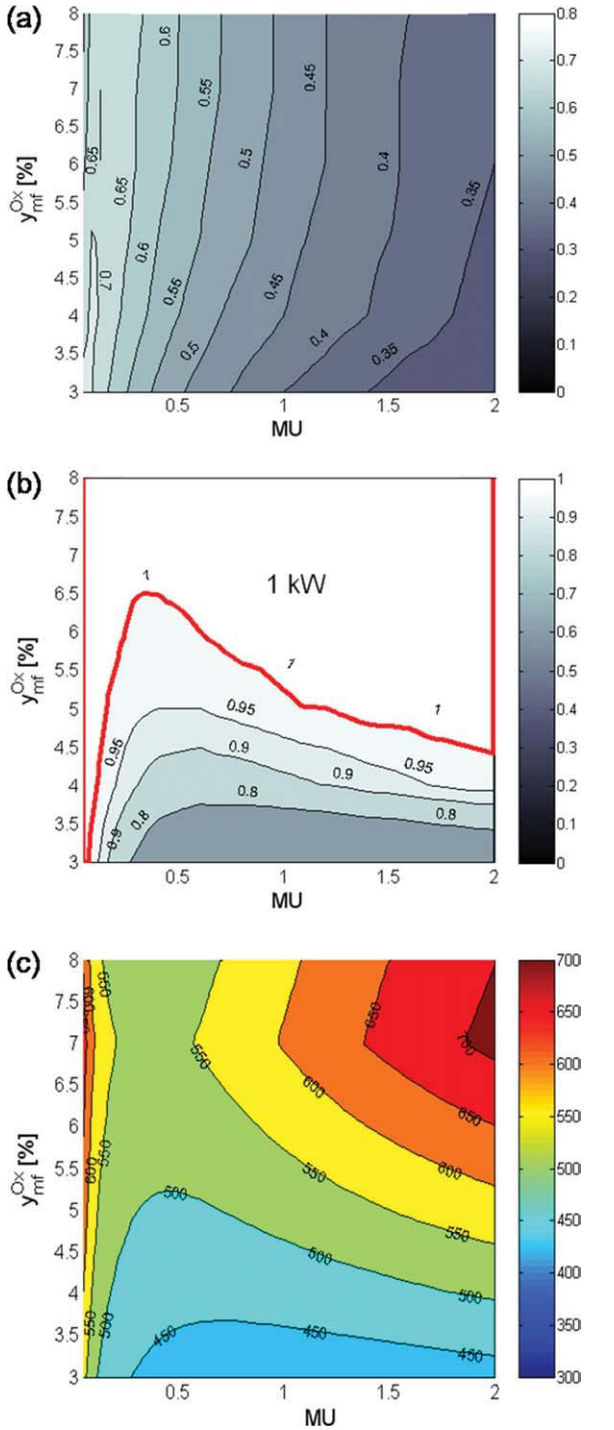

Figure 16. Reformer performance predicted by analytical approximation; 1 kW unit, recycle operation (Eq. 43): (a) efficiency (η), (b) power output (P) and average temperature (T_{av}). $Q_{mf}^{SR} = 2.4$ NL/min, $P_t^{SR/M} = 1/0.1$ MPa, $4Pe_M^* = 0.2$, dimensions listed in Table 3.

[Color figure can be viewed in the online issue, which is available at wileyonlinelibrary.com.]

Conclusions

Autothermal membrane packed bed reformer (ATMPBR) for hydrogen generation by steam reforming of methane has been studied theoretically, using a comprehensive numerical model and an approximate analytical solution and capitalizing on the experimental data, to optimize the reformer power output and efficiency. The reformer comprises of two separate catalytic packed bed compartments for methane oxidation (Ox) and steam reforming (SR), with heat exchange between them, and hydrogen separation membranes for extraction hydrogen generated in the steam reforming bed. Performing methane oxidation in an adjacent fixed bed allows for operating the reformer autothermally, while the operating parameters of the reforming and oxidation processes can be relatively independently adjusted. Simultaneous hydrogen separation by Pd-Ag hydrogen perm-selective membranes shifts the SR equilibrium, resulting in high methane conversions at relatively low temperatures, also providing extra-pure hydrogen that can be directly fueled to a PEMFC stack.

We first have developed an appropriate comprehensive model with no adjustable parameters (some of the parameters were estimated from the experimental data), solved it numerically, validated versus the experiments and then used it for the hydrogen generation optimization in terms of the reformer efficiency and power output. The problem then has been solved analytically, providing an analytical explicit approximation, and a thorough model-based optimization algorithm has been developed. A detailed parametric study, based on the experimental results, numerical simulations and kinetics and thermodynamics considerations, has been performed and the design limits have been determined.

The optimized reformer, with optimized hydrogen separation area, exothermic-to-endothermic feed ratio and reduced heat loss was shown to be suitable for fueling kW-range PEMFC stacks, providing a methane-to-hydrogen conversion efficiency of up to 0.8 (which is expected to provide an overall methane-to-electrical power efficiency of a combined ATMPBR-PEMFC unit of $\sim$0.5) and a volume power density of $\sim$1 kW/L. Recycling SR effluent with subsequent combustion of unreacted and unseparated compounds in the Ox bed is expected to provide an additional gain in terms of process efficiency.

Although the results for steady operation are encouraging, several dynamic problems should be considered. System start-up is a crucial issue, particularly for on demand power generation units. To ignite the reformer, it first has to be heated to the methane ignition temperature ($\sim$450°C). It may be done by an electrical heater, while there is no need to heat up the whole reformer. Raising temperature to the ignition limit over a narrow zone at the reactor entrance should send a front that heats the whole reactor. The implications for battery size should be checked. The ignition may be assisted by the addition of low light-off temperature hydrocarbons to the Ox feed (e.g., ethylene ignites at $\sim$150°C over the Pt/Al_2O_3 catalyst used in this study).

The integration with a PEMFC stack under conditions of varying power demand is more problematic. Yet, changes in the required hydrogen supply may be responded simply by varying SR methane feed flow rate, while the corresponding change in enthalpy is compensated by varying Ox methane feed flow rate, to provide an optimal thermal management of the reformer. With the design of indirect thermal coupling, the parameters of the Ox and SR compartments can be independently adjusted. The optimization algorithm we have developed allows for calculating the required feed rates. Obviously, in an autonomous system, a process control will be eventually required to assure proper operation and to prevent reactor extinctions and runaways.

Notation

A_j = pre-exponential of the rate coefficient of a reaction j[25]
A^k_{cs} = cross-sectional area of a compartment k
A_{H_2} = membrane permeability to hydrogen, mol/(m^2 s bar$^{0.5}$)
B_i = pre-exponential of the adsorption coefficient of a specie i[25]
Bi_s = wall-to-solid heat transfer Biot number
C_{pg} = gas heat capacity, kJ/(mol K)
d_p = particle diameter, m
d_t = tube diameter, m
d_w = wall thickness, m
D^k = diameter of a compartment k
D_{ax} = effective axial mass dispersion, m^2/s[28]
D_e = effective gas intraparticle diffusivity, m^2/s
D_m = gas molecular diffusivity, m^2/s
Da_{SR} = SR Damköhler number, Eq. 28
E_j = activation energy for a reaction j, kJ/mol[25]
E_{H_2} = H_2 separation activation energy, kJ/mol
f = conversion
F = molar flow rate, mol/s
ΔG = Gibbs free energy, kJ/mol
h_{fs} = fluid-solid heat transfer coefficient, kJ/(m^2 s K)
h_w = effective wall heat transfer coefficient, kJ/(m^2 s K)
HR = hydrogen recovery, Eq. 21
ΔH_j = heat of reaction j, kJ/mol
J_{H_2} = hydrogen flux, Ncm^3/(cm^2 min)
k_j = the rate coefficient of a reaction j[25]
K_i = the adsorption coefficient of a specie i[25]
k_{ax} = effective axial thermal conductivity, kJ/(m s K)
k_c = fluid-solid mass transfer coefficient, m/s
$K_{eq,j}$ = equilibrium constant of a reaction j
k_g = gas thermal conductivity, kJ/(m s K)
k_w = wall thermal conductivity, kJ/(m s K)
L = reactor length, m
MU = methane utilization, Eq. 24
Nu_w = wall heat transfer Nusselt number ($h_w d_p$ / k_g)
p_i = partial pressure of a specie i, MPa
P = power (Eq. 22), W
P_t = total pressure, MPa, bar
Pe = axial Peclet number ($\varepsilon(v\rho C_p)_g\, L/k_{ax}$)
Pe_M = membrane Peclet number, Eq. 20
Q_{tf} = total volumetric feed flow rate, m^3/s
R_h = hydraulic radius (V_p/S_p), m
R_j = rate of a reaction j
R_g = gas constant
Re_p = particle Reynolds number ($\rho_g v_g d_p/\mu_g$)
S^k = external surface of a reactor compartment k
S^M = membrane area, m^2
SV = space velocity ($3600Q^k_{tf}/[(1-\varepsilon)V^k]$), h^{-1}
t = time, h
T = temperature, °C, K
T_a = ambient temperature (25°C)
T_{av} = average temperature (Eq. 34a)
U_w = overall effective heat transfer coefficient (Eq. 11), kJ/(m s K)
v_g = gas velocity, m/s
V^k = volume of a compartment k, m^3
y_i = molar fraction of a specie i
z = axial reactor coordinate, m

Greek letters

α_{ij} = the stoichiometric coefficient of a specie i in a reaction j
α_v = surface-to-volume ratio, m^{-1}
δ = correction factor for incomplete SR and WGS converisons
ε = catalytic bed porosity

ϕ_i = the extent of a specie i
ϕ_j = Thiele Modulus of a reaction j
η = hydrogen production efficiency (HR/3.32)
η_j = effectiveness factor of a reaction j
μ_g = gas viscosity, (N s)/m^2
ρ_g = gas density, mol/m^3
ρ_s = solid density, kg/m^3
τ = residence time, s
τ_b = bed tortuosity
ξ = dimensionless reactor coordinate (z/L)

Subscripts

av = average
eff = effluent
f = feed
g = gas
HE = heat exchange
HL = heat loss
int = initial
m = methane
max = maximal
M = membrane
p = particle
t = total
s = solid
w = wall

Superscripts

M = membrane compartment
Ox = oxidation compartment
SR = steam reforming compartment

Abbreviations

FBMR = fluidized bed membrane reactor
FC = fuel cell
MOx = methane oxidation
MSR = methane steam reforming
PBMR = packed bed membrane reactor
PEM = polymer electrolyte membrane
Ox = oxidation
SR = steam reforming

Literature Cited

1. Johannessen E, Jordal K. Study of a H_2 separating membrane reactor for methane steam reforming at conditions relevant for power processes with CO_2 capture. *Energy Convers Manage*. 2005;46:1059–1071.
2. Bottino A, Comite A, Capannelli G, Di Felice R, Pinacci P. Steam reforming of methane in equilibrium membrane reactors for integration in power cycles. *Catal Today*. 2006;118:214–222.
3. Caravella A, Di Mario FP, Di Renzo A. Optimization of membrane area and catalyst distribution in a permeative-stage membrane reactor for methane steam reforming. *J Membr Sci*. 2008;321:209–221.
4. Abashar MEE, Alhabdan FM, Elnashaie SSEH. Staging distribution of oxygen in circulating fast fluidized-bed membrane reactors for the production of hydrogen. *Ind Eng Chem Res*. 2007;46:5493–5502.
5. Patel KS, Sunol AK. Modeling and simulation of methane steam reforming in a thermally coupled membrane reactor. *Int J Hydrogen Energy*. 2007;32:2344–2358.
6. Simakov DSA, Sheintuch M. Design of a thermally balanced membrane reformer for hydrogen production. *AIChE J*. 2008;54:2735–2750.
7. Gallucci F, Paturzo L, Fama A, Basile A. Experimental study of the methane steam reforming reaction in a dense Pd-Ag membrane reactor. *Ind Eng Chem Res*. 2004;4:928–933.
8. Tong J, Su L, Kashima Y, Shirai R, Suda H, Matsumura Y. Simulteneously depositing Pd-Ag membrane on asymmetric porous stainless steel tube and application to produce hydrogen from steam reforming of methane. *Ind Eng Chem Res*. 2006;5:648–655.
9. Mori N, Nakamura T, Noda K, Sakai O, Takahashi A, Ogawa N, Sakai H. Reactor configuration and concentration polarization in methane steam reforming by a membrane reactor with a highly hydrogen-permeable membrane. *Ind Eng Chem Res*. 2007;46:1952–1958.
10. Chen Y, Wang Y, Xu H, Xiong G. Efficient production of hydrogen from natural gas steam reforming in palladium membrane reactor. *Appl Catal B Environ*. 2008;80:283–294.
11. Patil CS, van Sint Annaland M, Kuipers JAM. Experimental study of a membrane assisted fluidized bed reactor for H_2 production by steam reforming of CH_4. *Chem Eng Res Des*. 2006;84:399–404.
12. Patil CS, van Sint Annaland M, Kuipers JAM. Fluidized membrane reactor for ultrapure hydrogen production via methane steam reforming: experimental demonstration and model validation. *Chem Eng Sci*. 2007;62:2989–3007.
13. Gallucci F, van Sint Annaland M, Kuipers JAM. Autothermal reforming of methane with integrated CO_2 capture in a novel fluidized bed membrane reactor I. Experimental demonstration. *Top Catal*. 2008;51:133–145.
14. Chen Z, Grace JR, Lim CJ, Li A. Experimental studies of pure hydrogen production in a commercialized fluidized-bed membrane reactor with SMR and ATR catalysts. *Int J Hydrogen Energy*. 2007;32:2359–2366.
15. Mahecha-Botero A, Boyd T, Gulamhusein Ali, Comyn N, Lim CJ, Grace JR, Shirasaki Y, Yasuda I. Pure hydrogen generation in a fluidized-bed membrane reactor: experimental findings. *Chem Eng Sci*. 2008;63:2752–2762.
16. Sznejer GA, Efremenko I, Sheintuch M. Carbon membrane for high-temperature gas separation: experiments and theory. *AIChE J*. 2004;50:596–610.
17. Zhang X, Hu H, Zhu Y, Zhu S. Methanol steam reforming to hydrogen in a carbon membrane reactor system. *Ind Eng Chem Res*. 2006;45:7997–8001.
18. Brunetti A, Barbieri G, Drioli E, Lee KH, Sea B, Lee DW. WGS reaction in a membrane reactor using a porous stainless steel supported silica membrane. *Chem Eng Process*. 2007;46:119–126.
19. Lee D, Zhang L, Oyama ST, Niu S, Saraf RF. Synthesis, characterization, and gas permeation properties of a hydrogen permeable silica membrane supported on porous alumina. *J Membr Sci*. 2004;231:117–126.
20. Casanave D, Ciavarella P, Fiaty K, Dalmon JA. Zeolite membrane reactor for isobutene dehydrogenation: experimental results and theoretical modeling. *Chem Eng Sci*. 1999;54:2807–2815.
21. Illgen U, Schäfer R, Noack M, Kölsch P, Kühnle A, Caro J. Membrane supported catalytic dehydrogenation of iso-butane using an MFI zeolite membrane reactor. *Catal Commun*. 2001;2:339–345.
22. Giaconia A, de Falco M, Caputo G, Grena R, Tarquini P, Marrelli L. Solar steam reforming of natural gas for hydrogen production using molten salt heat carriers. *AIChE J*. 2008;54:1932–1944.
23. Simakov DSA, Sheintuch M. Demonstration of a scaled-down autothermal membrane methane reformer for hydrogen generation. *Int J Hydrogen Energy*. 2009;34:8866–8876.
24. Simakov DSA, Sheintuch M. Experimental optimization of an autonomous scaled-down methane membrane reformer for hydrogen generation. *Ind Eng Chem Res*. 2010;49:1123–1129.
25. Xu J, Froment GF. Methane steam reforming, methanation and water-gas-shift. I. Intrinsic kinetics. *AIChE J*. 1989;35:88–103.
26. Trimm DL, Lam C-W. The combustion of methane on platinum-alumina fiber catalysts. I. Kinetics and mechanism. *Chem Eng Sci*. 1980;35:1405–1413.
27. Froment GF, Bischoff KB. *Chemical Reactor Analysis and Design*, New York: Wiley, 1979.
28. Anderson JB. A criterion for isothermal behavior of a catalyst pellet. *Chem Eng Sci*. 1963;18:147–148.
29. Mears DE. Tests for transport limitations in experimental catalytic reactors. *Ind Eng Chem Process Des Dev*. 1971;10:541–547.
30. Dixon AG, Cresswell DL. Theoretical prediction of effective heat transfer parameters in packed beds. *AIChE J*. 1979;25:663–676.
31. Derkx OR, Dixon AG. Effect of the wall Nusselt number on the simulation of catalytic fixed bed reactors. *Catal Today*. 1997;35:435–442.
32. Berger RJ, Pérez-Ramírez J, Kapteijn F, Moulijn A. Catalyst performance testing: radial and axial dispersion related to dilution in fixed-bed laboratory reactors. *Appl Catal A Gen*. 2002;227:321–333.
33. Sheintuch M, Dessau RM. Observation, modeling and optimization of yield, selectivity and activity during dehydrogenation of isobutene and propane in a Pd membrane reactor. *Chem Eng Sci*. 1996;51:535–547.
34. Sheintuch M. Design of membranal dehydrogenation reactors: the fast reaction asymptote. *Ind Eng Chem Res*. 1998;37:807–814.

Appendix

A. Methane steam reforming (MSR) equilibrium in membrane reactor

The MSR equilibrium is represented by $R_{SR} = 0$ (Eq. 9c):

$$p_{CH_4} p_{H_2O}^2 - \frac{p_{H_2}^4 p_{CO_2}}{K_{eq,SR}} = 0 \tag{A1}$$

The extents for different species are defined as follows (here f denotes the equilibrium conversion):

$$\phi_{CH_4} = 1 - f, \quad \phi_{H_2O} = 2(1-f), \qquad \phi_{CO_2} = f$$

$$\phi_{H_2} = y_{H_2} \sum_i \phi_i = y_{H_2}(3 - 2f + \phi_{H_2}), \quad \phi_{H_2} = \frac{y_{H_2}(3-2f)}{(1-y_{H_2})}$$

$$\sum_i \phi_i = (3-2f) + \frac{y_{H_2}(3-2f)}{(1-y_{H_2})} = \frac{(3-2f)}{(1-y_{H_2})}$$

Equation A1 is then expressed in terms of f and y_{H_2} ($p_i = y_i P_t^{SR}$, $y_i = \phi_i / \sum_i \phi_i$) :

$$y_{CH_4} y_{H_2O}^2 - \frac{\left(P_t^{SR}\right)^2}{K_{ep}^{SR}} y_{H_2}^4 y_{CO_2} = 0 \tag{A2}$$

$$\frac{4(1-f)^3(1-y_{H_2})^3}{(3-2f)^3} - \frac{1}{K'} \frac{y_{H_2}^4 f (1-y_{H_2})}{(3-2f)} = 0, \quad K' = \frac{K_{eq}^{SR}}{\left(P_t^{SR}\right)^2} \tag{A3}$$

B. Hydrogen mol fraction spatial distribution in membrane reactor

Substitution of $f = ay^2 + by + c$ into Eq. 29 yields

$$\frac{d(4ay^2 + 4by + 4c - y/y_{mf})}{d\xi} = \frac{(8ay + 4b - 1/y_{mf})dy}{d\xi} = \frac{1}{Pe_M}\left(\sqrt{y} - \Phi\right) \tag{A4}$$

Eq. A4 is then rearranged and integrated using a new variable x:

$$x = \sqrt{y}, \quad x^2 = y, \quad dy = 2xdx$$

$$\int \frac{x(8ax^2 + 4b - 1/y_{mf})dx}{(x-\Phi)} = \frac{1}{2Pe_M} \int d\xi$$

$$\frac{8ax^3}{3} + 4a\Phi x^2 + (8a\Phi^2 + (4b - 1/y_{mf}))x + (8a\Phi^3 - (4b - 1/y_{mf})\Phi)\ln(x-\Phi) = \frac{\xi}{2Pe_M} + C \tag{A5}$$

The constant C is then found using the inlet condition $y(0) = y_e$; y_e is the equilibrium value for a closed system. The closed system equilibrium expression is obtained by the same approach as in A-1, but with $\phi_{H_2} = 4f$ and $y_e = 4f / (3 + 2f)$. Note that $\sqrt{y} > \Phi$ (hydrogen partial pressure in the SR compartment is higher than that in the membrane interior) has to be satisfied. The solution of $y(\xi)$ for $\Phi \to 0$, i.e., $P_t^{SR} \gg P_t^M$ (high SR operation pressure or/and applying vacuum in the membrane interior) is

$$\frac{8a}{3}(y^{3/2} - y_e^{3/2}) + (4b - 1/y_{mf})(\sqrt{y} - \sqrt{y_e}) = \frac{\xi}{2Pe_M} \tag{A6}$$

In terms of x Eq. A6 has a form of a cubic polynomial:

$$x^3 + \bar{a}x^2 + \bar{b}x + \bar{c} = 0 \tag{A7}$$

The solution can be written explicitly (Cardano's method):

$$x = u - \frac{p}{3u} - \frac{\bar{a}}{3} \tag{A8}$$

$$\bar{a} = 0, \quad \bar{b} = \frac{3(4b - 1/y_{mf})}{8a},$$

$$\bar{c} = \left(-x_e^3 - \frac{3(4b - 1/y_{mf})}{8a} x_e - \frac{3\xi}{16aPe_M}\right)$$

$$p = \bar{b} - \frac{\bar{a}^2}{3} = \bar{b}, \quad u = \sqrt[3]{-\frac{q}{2} \pm \sqrt{\frac{q^2}{4} + \frac{p^3}{27}}},$$

$$q = \bar{c} + \frac{2\bar{a}^3 - 9\bar{a}\bar{b}}{27} = \bar{c}$$

$$y = \left(u - \frac{\bar{b}}{3u}\right)^2, \quad u = \sqrt[3]{-\frac{\bar{c}}{2} \pm \sqrt{\frac{\bar{c}^2}{4} + \frac{\bar{b}^3}{27}}} \tag{A9}$$

Manuscript received Nov. 7, 2009, and revision received Mar. 17, 2010.